Department of Physics

Thesis for M.Sc degree

Detecting tiny magnetic field by a tunable SNAIL

איתור שדה מגנטי זעיר על ידי סנייל מתכוונן

August 13, 2022

Student:
Zeyu Wang (EG4547209)

Supervisor:
Dr. Michael Stern

Abstract

The detection and characterization of tiny magnetic fields is nowadays an essential tool in biology, chemistry and material science. Recently, there has been an intense experimental effort to improve various techniques in order to detect and measure the magnetic field produced by a small number of nanoparticles. The objective of this research is to develop a new experimental technique that will allow the dispersive detection of magnetic field with unprecedented signal to noise ratio. This technique relies on a nonlinear φ^3 element called SNAIL which is made tunable by introducing a symmetric SQUID in replacement of its α junction.

Contents

1 Background

1.1 Challenge for detecting a single spin

The detection and characterization of small magnetic fields is nowadays an essential tool used in biology, chemistry and material science. Recently, there has been an intense experimental effort to improve various techniques in order to detect and measure the magnetic field generated by a small number of magnetic nanoparticles. A well-known technique consists of measuring the flux generated by these nanomagnets across a superconducting circuit. In order to understand the limitations of this experimental technique, we will first calculate the magnetic flux created by a magnetic dipole $\vec{M}$ through the superconducting loop shown in Fig.1(a). The vector potential created by such a dipole is given by $\vec{A} = \frac{\mu_0}{4\pi}\vec{M} \times \frac{\vec{r}}{r^3}$. It is possible to calculate the flux of the magnetic dipole Φ_d through the circuit by Stokes' theorem:

$$\Phi_d = \iint \vec{B} \cdot d\vec{S} = \iint \nabla \times \vec{A} \cdot d\vec{S} = \oint \vec{A} \cdot d\vec{l}$$

Assuming that the wire forming the loop are thin enough , we obtain:

$$\Phi_d = \frac{\mu_0 M}{4\pi d}\left(\frac{1}{\sqrt{\frac{1}{4}+\left(\frac{d}{L}\right)^2}} - \frac{1}{\left[\left(\frac{L}{d}\right)^2+1\right]\sqrt{\frac{5}{4}+\left(\frac{d}{L}\right)^2}}\right) \approx \frac{\mu_0 M}{2\pi d} \qquad \frac{L}{d} \to \infty$$

where L is the diameter of the superconducting loop and d its distance to the nanomagnet. For a single electron spin ($M = \mu_B$) situated at a distance d=20 nm we get $\Phi_d \sim 50\, n\Phi_0$. In the following, we will show that this value is much smaller than the typical noise ($\gtrsim 1\, \mu\Phi_0$ *at* $1\, Hz$) of superconducting loops which explains why the detection of a single electron spin is so hard.

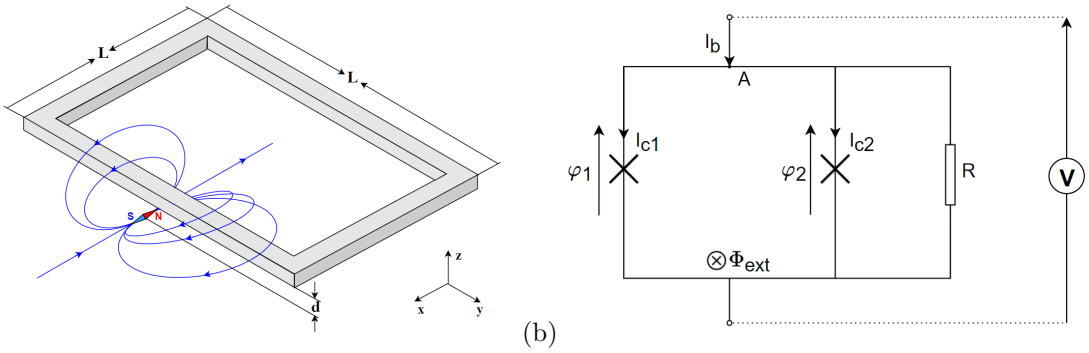

Figure 1: (a) Schematic picture showing a magnetic dipole $\vec{M}$ positioned at a distance d below a SQUID. (b) The equivalent electrical circuit of a DC-SQUID.

1.2 The DC SQUID

One of the most popular and established way to measure weak magnetic fields is to use a device called DC SQUID[1, 2]. This device (shown in Fig.1(b)) is formed by two Josephson junctions in parallel with a resistor R. During the measurement, a bias current I_b which value is set above the critical current of the junctions (I_{c1}+ I_{c2}) is applied on the circuit. The external magnetic field threading the SQUID loop Φ_{ext} is measured by the voltage difference V at the terminals of the resistor R. In the following, we will briefly explain the functioning of this device and its limitations.

1.2.1 Functioning of a DC SQUID

In order to understand the functioning of the circuit, we write the conservation of current at node A (see in Fig.1(b))

$$I_b = I_{c1}\sin\left[\varphi_1\right] + I_{c2}\sin\left[\varphi_2\right] + \frac{V}{R}$$

In this equation, φ_1 (resp.φ_2) is the superconducting phase difference across the Josephson junction with critical current I_{c1} (resp. I_{c2}) and V is the voltage difference across the resistor. Using Maxwell-Faraday equation $\dot{\Phi} = \iint \frac{\partial \vec{B}}{\partial t}\cdot d\vec{S} = -\oint \vec{E}\cdot d\vec{l}$, integrating over time and taking into account the second Josephson relation V= $\varphi_0\dot{\varphi}$, we obtain a relation between the phases φ_1, φ_2 and the external magnetic flux Φ_{ext}:

$$\varphi_1 - \varphi_2 = \frac{\Phi_{ext}}{\varphi_0}$$

where $\varphi_0 = \frac{\hbar}{2e}$ is the reduced magnetic flux quantum. In a balanced SQUID where the two junctions have identical critical currents $I_{c1} = I_{c2} = I_c$, the bias current I_b can therefore be rewritten as:

$$I_b = 2I_c\cos\left[\frac{\Phi_{ext}}{2\varphi_0}\right]\sin\left[\frac{\varphi_1+\varphi_2}{2}\right] + \frac{V}{R}$$

By introducing $\delta = (\varphi_1+\varphi_2)/2$, we get :

$$I_b = I_c(\Phi_{ext})\sin\delta + \frac{\varphi_0\dot{\delta}}{R}$$

where $I_c(\Phi_{ext}) = 2I_c\cos\left[\frac{\Phi_{ext}}{2\varphi_0}\right]$. By integrating this differential equation over a period, we get:

$$\int_0^T dt = \int_0^{2\pi} \frac{\varphi_0}{R(I_b - I_c(\Phi_{ext})\sin\varphi)}d\delta$$

$$T = \frac{2\pi\varphi_0}{R\sqrt{I_b^2 - I_c^2(\Phi_{ext})}}$$

The period T of the current flowing in the Josephson junction being related to the DC voltage at its terminals by $V/\varphi_0 = 2\pi/T$, we obtain:

$$V = R\sqrt{I_b^2 - I_c^2(\Phi_{ext})} = R\sqrt{I_b^2 - 2I_c^2\left(1+\cos\frac{\Phi_{ext}}{\varphi_0}\right)}$$

This equation shows that the DC voltage on the SQUID is a periodic function of the external flux Φ_{ext} of period $2\pi\varphi_0$. In the vicinity of $\Phi_{ext}/\varphi_0 = \frac{\pi}{2}$ and when bias current is slightly above the critical current of the junctions ($I_b \gtrsim 2I_c$), the behavior of the DC SQUID voltage is almost linear as a function of the external flux. The value of the flux-to-voltage coefficient is simply given by

$$V_\Phi = \frac{\partial V}{\partial \Phi_{ext}} \approx \frac{I_c R}{\sqrt{2}\varphi_0}$$

1.2.2 Noise limitations

Thermal noise One of the limiting factors of DC SQUID for detecting tiny magnetic flux are thermal fluctuations of the charge carriers inside the resistor R. Such noise -known as Johnson Nyquist noise- has an almost white spectral density and depends linearly on temperature

$$S_V(f) = 4k_BTR$$

By using the flux to voltage transfer coefficient V_Φ, we get the flux noise's spectral density due to thermal fluctuations:

$$S_\Phi(f) = S_V(f)/V_\Phi^2 \cong \frac{8k_BT\varphi_0^2}{I_c^2R}$$

For the typical values $R = 1\,\Omega$, $I_c = 1\,\mu A$ and $T = 4\,K$, we obtain a standard deviation of $3.35\,\mu\Phi_0$ when averaging over a bandwidth of 1 Hz. To increase further the signal to noise ratio ($50n\Phi_0/3.35\mu\Phi_0 \approx 0.015$) of this measurement, one can try to reduce the temperature. Yet, this method cannot hold all the way to $T = 0$ due to quantum corrections, which hinder the increase of sensitivity with temperature. The temperature dependence of $S_\Phi(f)$ was studied by Wellstood and coworkers in the 1990s [3, 4] by cooling SQUID to mK temperatures. It was found that the thermal noise falls linearly with temperature down to $T \sim 150\,mK$. Beyond this point, the power spectrum $S_\Phi(f)$ was found to be limited by another source of noise.

1/f noise Many experiments on SQUIDs [5, 4] have shown that an extra- flux noise which does not depend on temperature below 150 mK is always present and has a spectral density:

$$S_\Phi^{micro}(f) = A^2/f$$

One possible origin of this noise are random fluctuations of spins in the vicinity or at the surface of the SQUID loop [5]. These spins may be located in the thin oxide formed at the surface of the superconductor or inside the Josephson junctions themselves. In the following, we will try to explain briefly this phenomenon. Let's consider a large ensemble of spins situated in the close vicinity of the SQUID loop. Each spin can flip between its ground and excited state with a rate γ_n and modify the flux threading the SQUID loop by $\delta\Phi_n$. Assuming that the spin flips are independent, the total flux power spectrum created by these spin flips is given by[6, 7]:

$$S_\Phi^{micro}(f) = \Sigma_n S_n = \sum_n \frac{2\gamma_n\delta\Phi_n^2}{4\pi^2f^2 + \gamma_n^2}$$

When the number of spins is large enough, one can introduce a density of spins with a given flipping rate and consider in a first approximation that this density is uniformly distributed between γ_1 and γ_2 with probability $p(\gamma)$, the spectral density could be written as the integral:

$$S_\Phi^{micro}(f) = \int_{\gamma_2}^{\gamma_1} \frac{2\gamma p(\gamma)\left[\delta\Phi(\gamma)\right]^2}{4\pi^2f^2 + \gamma^2} d\gamma$$

Assuming that integrating coefficient $A^2 = \frac{1}{4}\gamma p(\gamma)\left[\delta\Phi(\gamma)\right]^2$ is independent of flipping rate γ and $\gamma_1/f \ll 1, \gamma_2/f \gg 1$, we get

$$S_{\Phi}^{micro}(f) = \frac{2A^2}{\pi f}\left[arctan\left(\frac{\gamma_2}{f}\right) - arctan\left(\frac{\gamma_1}{f}\right)\right] \approx \frac{A^2}{f}$$

The amplitude of A is found empirically and depends on the SQUID geometry [5]. It is typically in the range of $2-3\,\mu\Phi_0$[8, 9, 10]. and therefore much higher than the signal of a single spin in the condition described herein above. In order to reduce the effect of the $1/f$ noise and detect the spin signal, one can modulate it at frequency f_m and use lock in demodulation techniques to remove efficiently the noise. With such a technique, the bare SNR of a single spin is then given by:

$$SNR = 50\, n\Phi_0 / \sqrt{\int_{f_m}^{f_m+1/\tau} S(f)df} = \frac{50\, n\Phi_0}{A}\sqrt{f_m\tau} \approx 0.5$$

Assuming $f_m = 1KHz$ and the measurement time $\tau = 1s$.

In practice, the SNR of such a measurement is often reduced by the white noise of the amplifiers used to increase the amplitude of the signal and is given by:

$$SNR = \frac{50\, n\Phi_0 \cdot V_\Phi}{\sqrt{V_\Phi^2 \frac{A^2}{f_m\tau} + \frac{4k_BTR_0}{\tau}}} = \frac{50\, n\Phi_0\sqrt{\tau}}{\sqrt{\frac{A^2}{f_m} + \frac{8k_BTR_0\varphi_0^2}{I_c^2R^2}}}$$

Assuming that one uses a cryogenic state of the art HEMT amplifier with a noise temperature of $T = 4\ K$ and input impedance of $R_0 = 50\ \Omega$, we get $SNR \sim 0.002/\sqrt{Hz}$ which is far below our requirements.

1.3 SQUID-embedded CPW Resonator

Moreover, the continuous dissipation in the shunt resistor will produce local heating and a backaction that can potentially induce relaxation and decoherence of a nanoscale magnet. It is possible to eliminate such dissipation by using an unshunted SQUID embedded into a coplanar waveguide (CPW) resonator (see in Fig.2(a)) [11, 12, 13].

As for DC SQUID, our magnetometer consists of two elements: a flux to microwave signal transducer and a subsequent amplifier. The transducer is a coplanar waveguide resonator intersected at its midpoint by a SQUID. The SQUID acts as a flux dependent inductor. Thus an input signal threading the SQUID loop will result in a variation of the resonance frequency of the resonator. In the following, we will describe the functioning of this device and its limitations.

1.3.1 Functioning

As discussed in section 1.2.1, the SQUID behaves as a single junction with tunable critical current $I_c(\Phi_{ext}) = I_c(\Phi_{ext}) = 2I_c\cos\left[\frac{\Phi_{ext}}{2\varphi_0}\right]$. When the current fluctuations of the resonator are low compared to the critical current of the SQUID , the SQUID behaves as a flux-tunable inductor with an inductance

$$L_J(\Phi_{ext}) = \frac{\varphi_0}{2I_c\left|\cos\frac{\Phi_{ext}}{2\varphi_0}\right|}$$

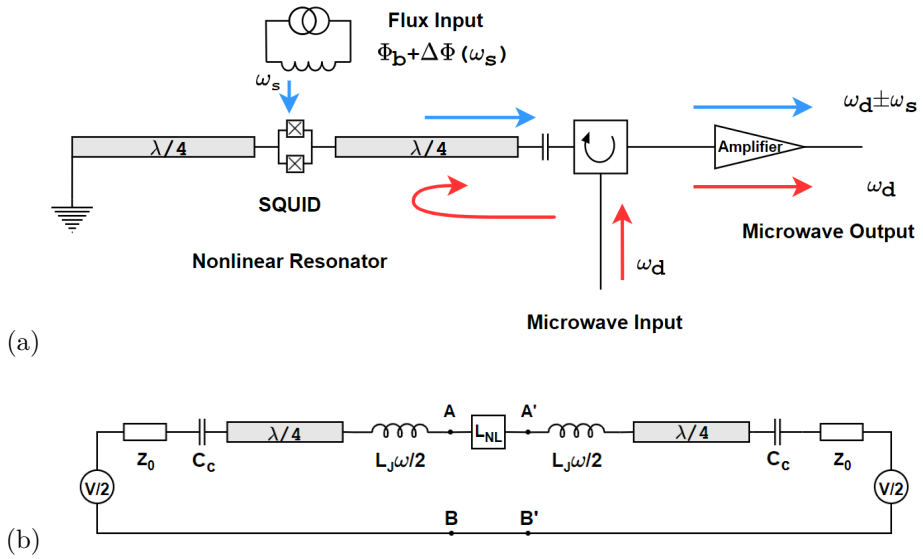

Figure 2: (a) Schematic picture showing SQUID-embedded CPW magnetometer detecting the modulated flux signal at frequency ω_s. The applied magnetic flux (blue arrows) modulate the frequency of CPW resonator and the amplitude of the modulation is detected as a certain shift in the frequency of a microwave drive signal (red arrows) reflected from the device. (b) Equivalent circuits of SQUID-embedded CPW resonator.

In practice, a SQUID has always a small level of asymmetry between the two junctions ($I_{c1} = (1+d)I_c$, $I_{c2} = (1-d)I_c$ $d \in (0,1)$), therefore the inductance will be described as:

$$L_J(\Phi_{ext}) = \frac{\varphi_0}{2I_c\sqrt{\frac{1+d^2+(1-d^2)\cos[\Phi_{ext}/\varphi_0]}{2}}}$$

Inserting this inductor in the middle of a $l = \lambda/2$ CPW resonator changes its resonance frequency from ω_1 (without SQUID) to $\omega_r(\Phi_{ext})$. To determine the frequency shift, we can split the SQUID into two series inductors $L_J/2$(shown in Fig.2(b)), the voltage at the middle point in-between the two inductors should be zero due to symmetry. Thus, the resonance frequency $\omega_r(\Phi_{ext})$ is equal to that of a $\lambda/4$ resonator shortcut to ground by an impedance $Z_L = iL_J(\Phi_{ext})\omega/2$. Now the input impedance seen from the coupling capacitor is given by:

$$Z_{in} = Z_0\frac{Z_L + iZ_0\tan[\beta l/2]}{Z_0 + iZ_L\tan[\beta l/2]}$$

where $\beta = \omega_r/\sqrt{L_l C_l}$ is the propagation constant in the CPW. Taking into account that when $\tan[\beta l/2] = -1/\tan[\pi(\omega_r-\omega_1)/2\omega_1]$, the resonance frequency is a pole of this input impedance and is therefore given by the equation

$$Z_0\tan\frac{\pi(\omega_r(\Phi_{ext})-\omega_1)}{2\omega_1} + \frac{L_J(\Phi_{ext})\omega_r(\Phi_{ext})}{2} = 0$$

Expanding to the first order the tangent terms, we can obtain the expression of resonance frequency (Shown in Fig.3(a) with $I_c = 15\,\mu A$, $Z_0 = 50\,\Omega$ and $f_1 = 3.75\,\mathrm{GHz}$).

$$f_r(\Phi_{ext}) \approx f_1\frac{\pi Z_0/\omega_1}{\pi Z_0/\omega_1 + L_J(\Phi_{ext})} = \frac{f_1}{1+\epsilon(\Phi_{ext})}$$

where $\epsilon(\Phi_{ext}) = \dfrac{\omega_1 L_J(\Phi_{ext})}{\pi Z_0}$.

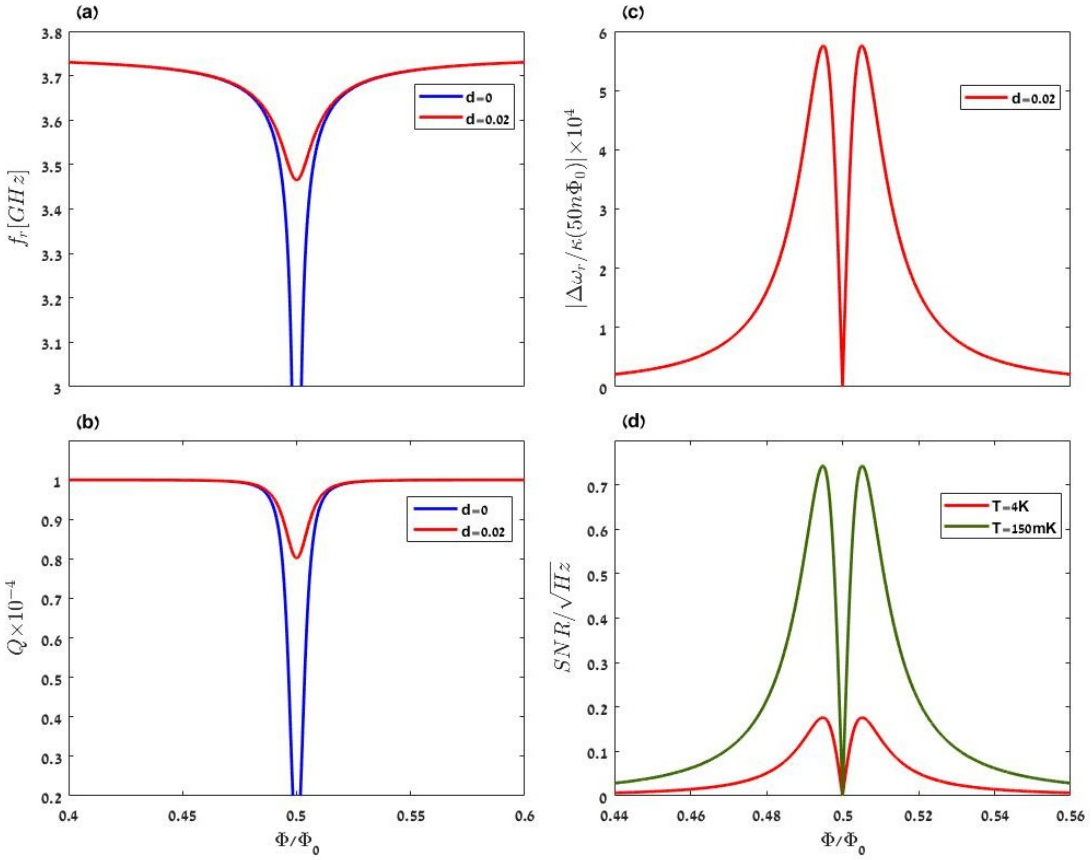

Figure 3: Using a SQUID-embedded CPW to detect magnetic field. (a) Frequency of the CPW resonator vs the DC magnetic flux threading the SQUID loop. The SQUID asymmetry is chosen to be $d = 0$ (in blue) or $d = 0.02$ (in red). (b) Quality factor of CPW resonator vs the magnetic field threading the loop of the SQUID. (c) Sensitivity of the resonance frequency ($\Delta\omega_r/\kappa$) to a flux of $50\,n\Phi_0$. (d) Signal to noise ratio (SNR) for a single photon in the resonator ($\bar{n}$=1) in presence of a cold HEMT amplifier with a noise temperature of 4K (in red) or in presence of a parametric Josephson amplifier with a noise temperature of $150\,mK$ (in green).

1.3.2 Limitations

Quality factor In the vicinity of $\Phi_0/2$ the effective critical current $I_c(\Phi_{ext})$ becomes very small, thus the non-linear component of L_J (shown in Fig.2(b)) cannot be neglected and induces Kerr non linearity. When $I_c(\Phi_{ext})$ becomes the same order small as the fluctuations of the current inside of the resonator, these fluctuations will induce a inhomogeneous broadening of the resonance $\delta\omega_r(\Phi_{ext})$ which can be represented by the equivalent inhomogeneous quality factor Q_{inh}:

$$Q_{inh}^{-1}(\Phi) = \frac{\delta\omega_r(\Phi_{ext})}{\omega_r(\Phi_{ext})} = -\left(\frac{2\omega_r(\Phi_{ext})}{\pi Z_0[1+2\epsilon(\Phi_{ext})]}\right)^2 \frac{\varphi_0}{8I_c^3(\Phi_{ext})}\delta\bar{E}$$

where the standard deviation of the resonator energy $\delta\bar{E}$ is given by

$$\delta\bar{E} = \delta\bar{n}\hbar\omega_r = \sqrt{\bar{n}}\hbar\omega_r$$

where $\bar{n}$ is the average number of photons in the resonator. This yields the total quality factor (shown in Fig.3(b)):

$$Q(\Phi_{ext}) = [Q_c^{-1} + Q_{inh}^{-1}(\Phi_{ext})]^{-1}$$

Therefore, the number of photons in the resonator should always be small if one wishes to avoid inhomogeneous effect linked to Kerr non linearity. Typically, the coupling quality factor Q_c is chosen to be high (10^4) to improve the magnetic flux detection. The sensitivity of the resonance frequency in response to the external flux shift (50 $n\Phi_0$) is approaching maximum when the external flux is close to 0.495 Φ_0 (shown in Fig.3(c)). The measured reflected signal amplitude is given by Input Output Theory[14, 15].

$$a_{out} = \frac{\kappa_c - \kappa_{inh} + 2i(\omega - \omega_r)}{\kappa_c + \kappa_{inh} - 2i(\omega - \omega_r)} a_{in}$$

$$Signal = \left|\frac{\Delta a_{out}}{a_{in}}\right|^2 P_{in} = \frac{16\Delta\omega^2\kappa_c^2}{[4\Delta\omega^2 + \kappa^2]\kappa^2} P_{in} \approx \frac{16\Delta\omega^2\kappa_c^2}{\kappa^4} P_{in}$$

In order to decrease the influence of the SQUID's Kerr non-linearity, the input power $P_{in} = \frac{1}{4}\hbar\omega_r\kappa^2\bar{n}/\kappa_c$ is always limited to a very low value. The signal to noise ratio with a HEMT amplifier can only approach $0.2/\sqrt{Hz}$ when the average photon number in the resonator is typically chosen to be 1. Even using a parametric Josephson amplifier to decrease the thermal noise, one can improve the SNR by a factor of 4 but still be far away from the requirements of detecting few spins.

Bifurcation In addition, the Kerr non linearity gives rise to a phenomenon of bistability of the SQUID-embedded CPW Resonator. In the following, we will briefly analyze the appearance of the bifurcation phenomena in our circuit by using an equivalent RLC model (shown in Fig.4(a)) which is formed by a capacitor $C_e = \frac{\pi}{2}\frac{Z_0}{\omega_r}$ in parallel with a resistor $R_e = \frac{2}{\pi}QZ_0$ and with a flux dependent inductor $L_t = L_e + L_J = \frac{\pi}{2}\frac{Z_0}{\omega_1} + \frac{\varphi_0}{I_c(\Phi_{ext})}$, driven by a current source $I(t) = I_m\cos(\omega_m t)$. The equation of motion of this circuit can be written as[16]

$$\frac{I_m}{I_c}\cos(\omega_m t) = \frac{\ddot{\delta}}{\omega_r^2} + \frac{1}{\omega_r Q}\dot{\delta} + sin\delta$$

where δ now represents the phase across SQUID and the renormalized resonance frequency of the circuit is given by $\omega_r = \sqrt{1/L_tC_e} = \frac{\omega_1}{1+L_J/L_e}$.

Give an ansatz that $\delta(t) = A\cos(\omega_m t + \varphi)$, we obtain:

$$-A\Omega^2\cos(\omega_m t + \varphi) - \frac{\Omega}{Q}A\sin(\omega_m t + \varphi) + \sin[A\cos(\omega_m t + \varphi)] = \eta\cos(\omega_m t)$$

where reduced driving amplitude $\eta = I_m/I_0$ and reduced frequency $\Omega = \omega_m/\omega_0$.

Using Bessel expansion $\sin(x\cos(y)) = -2\sum_n(-1)^n J_{2n-1}(x)\cos[(2n-1)y]$, we get:

$$\begin{cases} -A\Omega^2\cos(\varphi) - \dfrac{\Omega}{Q}A\sin(\varphi) + 2J_1(A)\cos(\varphi) = \eta \\ A\Omega^2\sin(\varphi) - \dfrac{\Omega}{Q}A\cos(\varphi) - 2J_1(A)\sin(\varphi) = 0 \end{cases}$$

Thus, the stationary solution should obey:

$$\eta^2 = \left(2J_1(A) - A\Omega^2\right)^2 + \left(\frac{\Omega}{Q}\right)^2 A^2 = \left((1-\Omega^2) - \frac{A^2}{8}\right)^2 + \left(\frac{\Omega}{Q}\right)^2 A^2$$

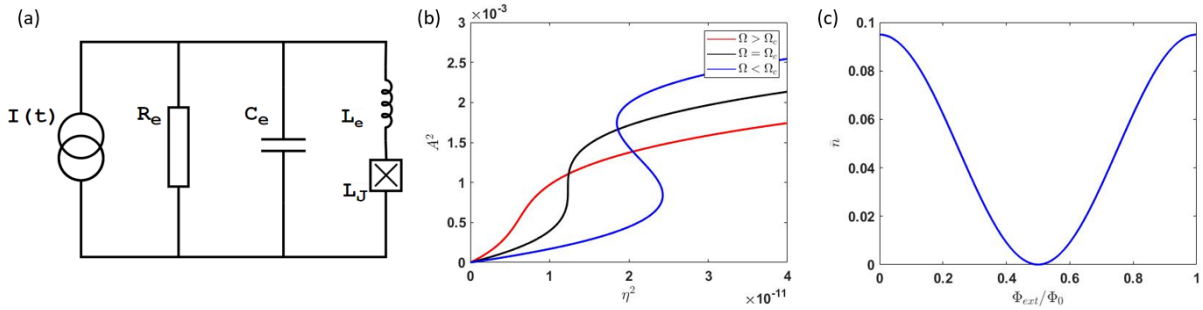

Figure 4: (a) Equivalent RLC circuits of SQUID-embedded CPW resonator. (b) Steady-state solutions of motion equation as a function of the drive $\eta^2 = I_m^2/I_0^2$ for different reduced frequency $\Omega = \omega_m/\omega_0$ while Q is typically chosen to be 10000. (c) The maximal number of photons $\bar{n}$ stored at bifurcation versus external magnetic flux.

The resonator's quality factor Q is typically chosen to be 10000. Depending on the (η, Ω) parameter range, the above equation has 1 or 3 solutions. The bifurcation point happens when $d\eta^2/dA^2 = 0$ and $d^2(\eta^2)/d(A^2)^2 = 0$. At this point, the number of photons $\bar{n}$ stored inside the resonator is limited at

$$\bar{n} = \left|\frac{2\sqrt{\kappa}}{\kappa - 2i(\omega_1 - \omega_r)}\right|^2 \frac{P_{in}}{\hbar\omega_r}$$

where $P_{in} = I_m^2 Z_0 = \eta^2 I_0^2 Z_0$.

2 Methodology

In order to improve the signal to noise ratio of detecting an essemble of few spins, one can pump the resonator strongly to increase the number of photons stored inside. However, as mentioned earlier this will affect the quality factor via the Kerr non-linearity (φ^4). Here we propose to replace the SQUID by a tunable Superconducting Nonlinear Asymmetric Inductive eLement (SNAIL)[17] which can be considered as a pure φ^3 nonlinear element.

2.1 Description of the SNAIL

The 'standard' non-tunable SNAIL [17, 18] consists of a superconducting loop threaded by an external magnetic flux Φ_{ext} and intersected by four Josephson junctions (shown in Fig.5(a)). Among these junctions, one is smaller than the others by a factor α. The proposed circuit has an inductive energy which is similar to the one of superconducting flux qubit[19, 20, 9, 10] :

$$U_{\text{SNAIL}} = -\sum_{i=1}^{3} E_J \cos(\varphi_i) - \alpha E_J \cos(\varphi_\alpha)$$

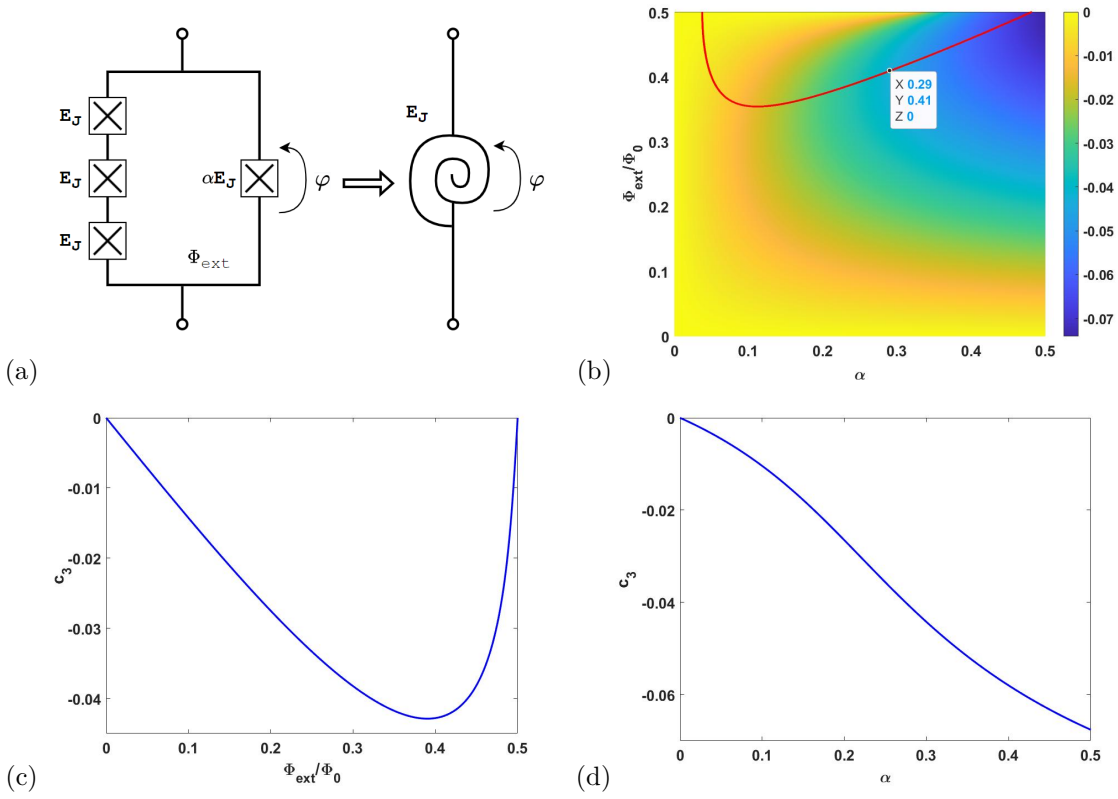

Figure 5: (a) Circuit diagram of a Superconducting Nonlinear Asymmetric Inductive eLement (SNAIL). The SNAIL is a superconducting loop threaded by a magnetic flux $\Phi_{ext}$and intersected by four Josephson junctions, one of which being smaller than the others by a factor α. (b) Third order non linearity c_3 versus α and Φ_{ext}. The red line represents the points where the fourth order non linearity c_4 is equal to zero. (c) Cross-section representing c_3 vs Φ_{ext} at $\alpha = 0.29$. (d) Cross section representing c_3 vs α at $\Phi_{ext} = 0.41$.

where $E_J = I_c\varphi_0$ is unitary junction's Josephson energy andφ_i the phase difference across each junction. The loop condition $\sum_{i=1}^{3}\varphi_i + \varphi_\alpha - \varphi_{ext} = 0$ and the fact that $E_J \gg \frac{e^2}{2C_J}$ and $C_0 \ll C_J$ (where C_J is the capacitance of the junction and C_0 is the capacitance to the ground) makes it possible to reduce the number of degrees of freedom and write U_{SNAIL} as :

$$U_{\text{SNAIL}} = -\alpha E_J \cos(\varphi) - 3E_J \cos\left(\frac{\varphi_{ext} - \varphi}{3}\right)$$

The main difference between a SNAIL and a flux qubit is the choice of the parameter α.In a flux qubit, α is chosen such that the potential has two degenerated minima while in a SNAIL, one chooses α such that there is always one single minimum in the potential energy. The position of the minimum is given by solving the partial differential equations:

$$\partial_\varphi U_{SNAIL}(\varphi_{min}) = \alpha E_J \sin(\varphi_{min}) - E_J \sin\left(\frac{\varphi_{ext} - \varphi_{min}}{3}\right) = 0$$

The Taylor expansions of SNAIL's potential close to this point is given by:

$$U_{SNAIL} = U_{SNAIL}(\varphi_{min}) + \sum_{m=1}^{\infty} \frac{1}{m!} \frac{\partial^m U_{SNAIL}(\varphi_{min})}{\partial \varphi^m} (\varphi - \varphi_{min})^m$$

Introducing $\tilde{\varphi} = \varphi - \varphi_{min}$, we get the effective potential:

$$U_{\mathbf{eff}}(\tilde{\varphi})/E_J = c_2\tilde{\varphi}^2 + c_3\tilde{\varphi}^3 + c_4\tilde{\varphi}^4 + \cdots$$

And

$$\begin{aligned}
c_2 &= \left(\alpha\cos(\varphi_{min}) + \frac{1}{3}\cos\left(\frac{\varphi_{ext} - \varphi_{min}}{3}\right)\right)/2 \\
c_3 &= \left(-\alpha\sin(\varphi_{min}) + \frac{1}{9}\sin\left(\frac{\varphi_{ext} - \varphi_{min}}{3}\right)\right)/6 \\
c_4 &= \left(-\alpha\cos(\varphi_{min}) - \frac{1}{27}\cos\left(\frac{\varphi_{ext} - \varphi_{min}}{3}\right)\right)/24
\end{aligned}$$

One can then choose a set of parameters α and Φ_{ext}, where $c_3 \neq 0$ and thus without Kerr effect up to sixth order.

2.2 Tunable SNAIL

In this work, we replace the small junction of the SNAIL with a symmetric SQUID which functions as a flux dependent Josephson junction. The external magnetic flux $\Phi_{ext,snail}$ and $\Phi_{ext,squid}$ are threading through the loops of SNAIL and SQUID respectively (shown in Fig.6). The potential energy of the system is given by:

$$U_{\text{SNAIL}} = -E_{J,squid,1}\cos(\varphi) - E_{J,squid,2}\cos(\varphi + \varphi_{ext,squid}) - 3E_{J,snail}\cos\left(\frac{\varphi_{ext,snail} - \varphi}{3}\right)$$

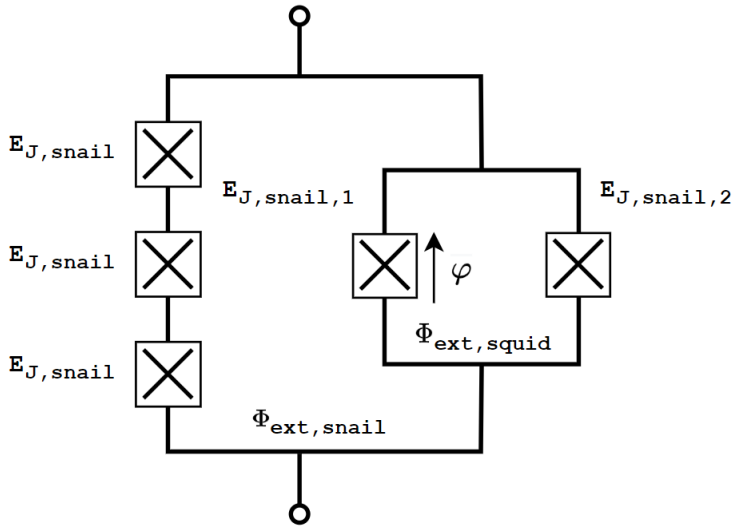

Figure 6: Circuit diagram for a tunable SNAIL consists of 3 unitary Josephson junctions and a SQUID.

As discussed in section 1.3.1, a SQUID always has a small level of asymmetry between the two junctions, therefore the potential will be described as:

$$U_{\text{SNAIL}} = -2E_{J,squid}\sqrt{\frac{1+d^2+(1-d^2)\cos(\varphi_{ext,squid})}{2}}\cos\left(\varphi+\delta\right) - 3E_{J,snail}\cos\left(\frac{\varphi_{ext,snail}-\varphi}{3}\right)$$

where $\delta = \dfrac{\varphi_{ext,squid}}{2} + \arctan\left(d\tan\left(\dfrac{\varphi_{ext,squid}}{2}\right)\right)$. Note $\varphi^\star = \varphi + \delta$, we can see that the potential has the form as above:

$$U_{\text{SNAIL}} = -2E_{J,squid}\sqrt{\frac{1+d^2+(1-d^2)\cos(\varphi_{ext,squid})}{2}}\cos\left(\varphi^\star\right) - 3E_{J,snail}\cos\left(\frac{\varphi_{ext,snail}+\delta-\varphi^\star}{3}\right)$$

2.3 SNAIL-embedded CPW Resonators

2.3.1 Lagrangian formulation and linearization

Figure 7 represents the equivalent circuit diagram of $\lambda/2$ CPW resonator with a SNAIL inserted at position $x_s/\lambda = 0.166$ of the center conductor. We note C_l and L_l capacitance and inductance per unit length respectively. The current $I(x,t)$ and voltage $V(x,t)$ inside CPW are given by:

$$V\left(x,t\right) = \partial_t \Phi(x,t)$$

$$I\left(x,t\right) = \frac{1}{L_l}\partial_x \Phi(x,t)$$

where $\Phi(x,t)$ is the generalized flux at the position x of the CPW.

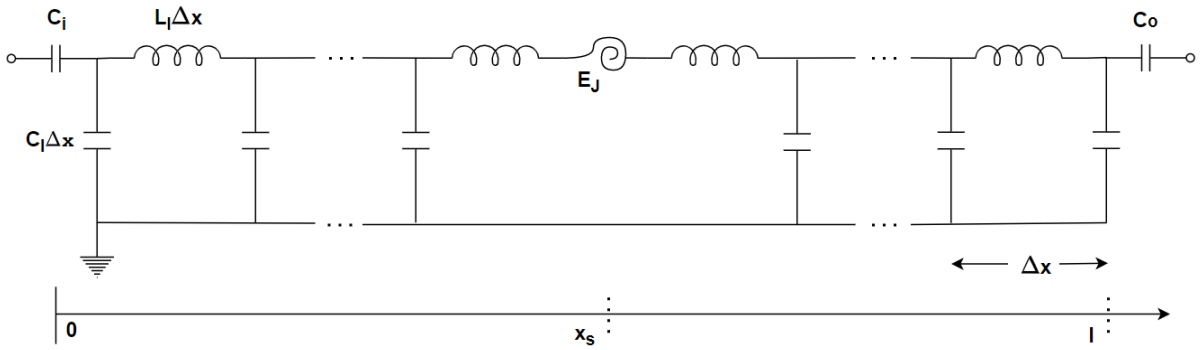

Figure 7: Discretized representation of a one port CPW resonator and with a SNAIL interrupting the center conductor at position x_s .

The Lagrangian of the system can be written as::

$$\mathcal{L} = \frac{1}{2}\int_0^l \left(C_l V^2 - L_l I^2\right) dx - U_{SNAIL} = \frac{1}{2}\int_0^l \left(C_l(\partial_t \Phi(x,t))^2 - \frac{1}{L_l}\left(\partial_x \Phi(x,t)\right)^2\right) dx - U_{SNAIL}$$

where the potential of the SNAIL is

$$U_{SNAIL} = E_J \sum_{m\geq 2} C_m \tilde{\varphi}^m$$

The phase difference across the SNAIL is given by

$$\tilde{\varphi} = [\Phi(x_s^+, t) - \Phi(x_s^-, t)]/\varphi_0$$

It's useful to extract the SNAIL's quadratic energy term functioning as a linear inductance L_s threaded with flux $\varphi_0\varphi$ while other higher order terms treated as a nonlinear potential[21]:

$$L = L_{CPW} - \frac{(\varphi_0\varphi)^2}{L_s} - E_J \sum_{m\geq 3} C_m \varphi^m \equiv L_L - U_{NL}(\varphi)$$

2.3.2 Normal modes decomposition

In order to analyze the normal modes stored in such linearized resonator, we first derive the Euler-Lagrange equation of motions

$$\sum_{\nu=x,t} \partial_\nu \left\{\frac{\partial L}{\partial[\partial_\nu \Phi(x,t)]}\right\} - \frac{\partial L}{\partial \Phi(x,t)} = 0$$

Away from the SNAIL and the resonator ports, the motion equation obeys the standard wave equation

$$\ddot{\Phi}(x,t) = v^2 \partial_{xx} \Phi(x,t)$$

where $v = 1/\sqrt{L_l C_l}$ is the light speed through the CPW. It's effective to decompose the flux $\Phi(x,t)$ into an infinite number of stationary wave modes with $\Phi_m(t)$ oscillating at the mode frequency ω_m.

$$\Phi(x) = \sum_{m=1}^{\infty} \Phi_m(t) u_m(x)$$

And the mode basis function $u_m(x)$ obeys general trigonometric form with wave vector k_m:

$$u_m(x) = \begin{cases} A_m \cos(k_m x + \varphi_i) & 0 \leqslant x \leqslant x_s^- \\ B_m \cos\left[k_m(x-\ell) + \varphi_f\right] & x_s^+ \leqslant x \leqslant \ell \end{cases}$$

The phases of the CPW's ends are determined by the boundary current condition $\partial_x \Phi(x,t)/L_l = 0$ $(x = 0, l)$. And the two capacitors on both ends can be viewed to a first approximation as perfect mirrors for the voltage waves while the CPW now forms as a cavity. Thus

$$\varphi_i = 0 \qquad \varphi_f = m\pi$$

Moreover, the current among the SNAIL still requires a continuum, which leads to

$$\frac{1}{L_l}\partial_x \Phi(x_s^-, t) = \frac{1}{L_l}\partial_x \Phi(x_s^+, t) = \frac{\varphi_0 \varphi}{L_s}$$

Hence, the ratio between A_m and B_m meets the first equality of above equation

$$\frac{B_m}{A_m} = \frac{\sin(k_m x_s)}{\sin\left[k_m(x_s - \ell) + m\pi\right]}$$

The eigenvalue equation for the wave vectork_m is numerically derived by inserting the second equality

$$\frac{k_m L_s}{L_l} = \cot(k_m x_s) - \cot\left[k_m(x_s - \ell) + m\pi\right]$$

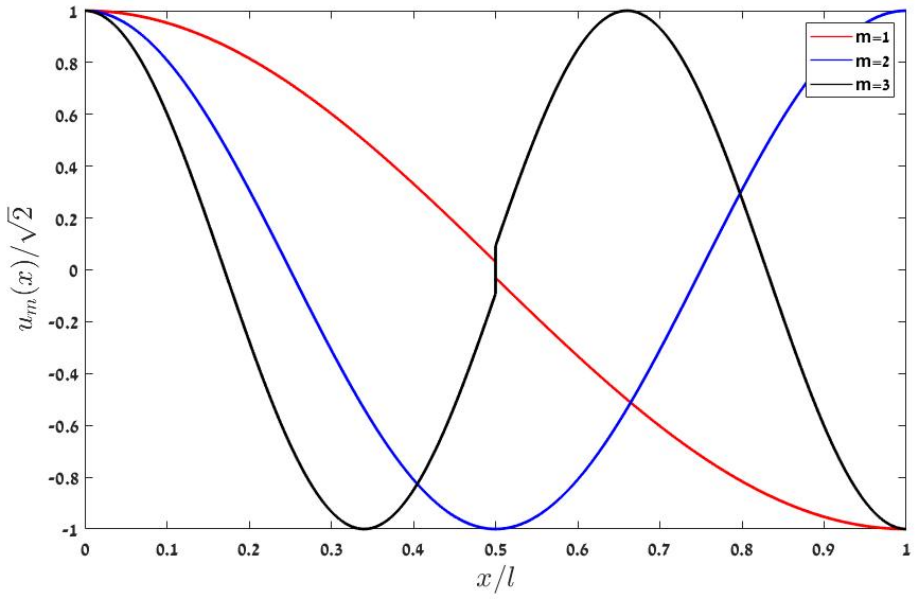

Figure 8: Typical diagram of the first three normal modes of a CPW resonator with a SNAIL at $x_s = l/2$.

Figure 8 typically presents the distribution of first three modes in the CPW with a SNAIL inserted in the middle. The odd modes' phases behave saltations at SNAIL's position while the even modes maintain continuum due to symmetry. It's possible for us to reach the proposed coupling for particular modes by modulating the position of the SNAIL.

Finally, the normalization parameter A_m is set by introducing the inner product of orthogonal mode

$$\langle u_m \cdot u_n \rangle \equiv \int_0^l C_l u_m(x) u_n(x) dx = C_t \delta_{mn}$$

and $C_t = \int_0^l C_l dx$ is the total capacitance. Similarly, we could define the inner product of modes' derivatives as they are required to obey orthogonality conditions:

$$\langle \partial_x u_m \cdot \partial_x u_n \rangle \equiv \int_0^l \frac{\partial_x u_m(x) \partial_x u_n(x)}{L_l} dx + \frac{\Delta u_m \Delta u_n}{L_s} = \frac{\delta_{mn}}{L_m}$$

where $\Delta u_m = u_m(x_s^+) - u_m(x_s^-)$ relates to the mode amplitude difference across the SNAIL. Thus we define the effective inductance of the resonator's mth mode as well as take into account the SNAIL inductance effect. The full expression of the linearized Lagrangian is given by

$$L_L = \sum_m \frac{C_t}{2} \dot{\Phi}_m^2 - \frac{\Phi_m^2}{2L_m}$$

2.3.3 Quantization of the Hamiltonian

Following the last section, we yield the system's Hamiltonian through Legendre transformation

$$H = \sum_m \dot{\Phi}_m \frac{\partial L}{\partial \dot{\Phi}_m} - L = \sum_m \frac{Q_m^2}{2C_t} + \frac{\Phi_m^2}{2L_m} + U_{NL}(\delta)$$

And in terms of the decomposed mode, the nonlinear potential takes the form

$$U_{NL}(\delta) = E_J \sum_{m \geq 3} C_m \left(\frac{\delta}{\varphi_0} \right)^m = E_J \sum_{m \geq 3} \frac{C_m}{\varphi_0^m} \left(\sum_k \Phi_k \Delta u_k \right)^m$$

To deal with the term $\Delta u \neq 0$, it's convenient to introduce the rescaled conjugate variables $\phi_m = \Phi_m \Delta u_m$ and $q_m = Q_m / \Delta u_m$. In this expression, the new Hamiltonian could be written as

$$H = \sum_m \left(\frac{q_m^2}{2C'_m} + \frac{\phi_m^2}{2L'_m} \right) + U_{NL}(\sum_m \phi_m)$$

while $L'_m = L_m \Delta u_m^2$ and $C'_m = C_t / \Delta u_m^2$ which obeys the same mode frequency. Quantize the Hamiltonian by introducing the creation and annihilation operators ($\hat{a}_m^\dagger$, $\hat{a}_m$) in mth mode:

$$\hat{\phi}_m = \sqrt{\frac{\hbar}{2C'_m \omega_m}} (\hat{a}_m + \hat{a}_m^\dagger) \qquad \hat{q}_m = i \sqrt{\frac{\hbar C'_m \omega_m}{2}} (\hat{a}_m^\dagger - \hat{a}_m)$$

Thus, we can rewrite the linearized Hamiltonian in the form of harmonic oscillators:

$$\hat{H_L} = \sum_m \hbar \omega_m \left(\hat{a}_m^\dagger \hat{a}_m + \frac{1}{2} \right)$$

and the nonlinear potential with the term

$$U_{NL} = E_J \sum_{m\geq 3} \frac{C_m}{\varphi_0^m} \left[\sum_k \sqrt{\frac{\hbar}{2C'_k\omega_k}} (\hat{a}_k + \hat{a}_k^\dagger) \right]^m = \sum_{m\geq 3} K_m \left[\sum_k A_k (\hat{a}_k + \hat{a}_k^\dagger) \right]^m$$

2.4 Simulation

Here, we compare the two different techniques described herein above i.e.SQUID-embedded CPW resonator versus tunable SNAIL-embedded CPW resonator. The dynamics of both systems can be well described by using Langevin equation of motion:

$$\dot{a} = -i\omega_1 a - \frac{\kappa_a}{2} a + \sqrt{\kappa_a} a_{in}(t)$$

where a is the intra-resonator mean field of the first mode, κ_a is the related loss rate and $a_{in}(t)$ is corresponding to the input power $P_{in}(t) = P_{in} cos\omega_m t$. By substituting the ansatz $a(t) = \alpha e^{-i\omega_m t}$ into our equation of motion , we get:

$$-i\omega_m \alpha = -i\omega_1 \alpha - \frac{\kappa_a}{2}\alpha + \sqrt{\kappa_a}\sqrt{\frac{P_{in}}{\hbar\omega_m}}$$

This yields the amplitude of the intra-resonator mean field as:

$$\alpha = \frac{2\sqrt{\kappa_a}}{\kappa_a - 2i(\omega_m - \omega_1)} \sqrt{\frac{P_{in}}{\hbar\omega_m}}$$

The output signal will approach the maximum when the drive frequency is tuned at the resonance frequency $\omega_m = \omega_1$. By introducing a time dependent flux inside the SNAIL, the resonance frequency shifts to:

$$\omega_1 = \omega_1^* + f(A, \omega_d, t)$$

where ω_1^* is resonance frequency with the DC bias magnetic flux, A is the intensity of the AC flux and ω_d is the oscillating frequency.

Thus, we can get the power spectrum of a from numerical simulation (codes shown in Appendix):

$$\alpha = \alpha_0(\omega_1^*) + \delta\alpha(A, \omega_d)$$

And the signal to noise ratio is given by:

$$SNR = \sqrt{\frac{2\left|\delta\alpha\right|^2}{n_{Thermal}}} = \sqrt{\frac{\hbar\kappa_a\omega_1^*\left|\delta\alpha\right|^2}{8k_BT}}$$

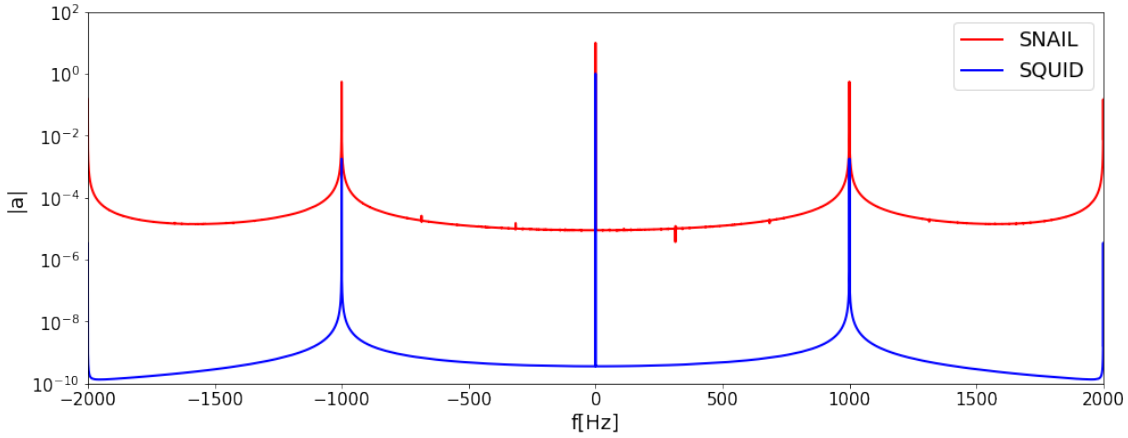

Figure 9: The blue curve shows the distribution of the the first mode of SQUID-embedded resonator with versus frequency away from the resonance ($\bar{n} = 1$). And the red curve shows the distribution of the the first mode of SNAIL-embedded resonator versus frequency away from the resonance ($\bar{n} = 100$). The parameters are typically set as : $\omega_1^* = 2\pi * 3.391\, GHz$, $\omega_d = 2\pi * 1\, kHz$, $A = 50\, n\Phi_0$ and $Q = 10000$.

As discussed in section 1.3.2, the bifurcation point will limit the number of photons stored inside the resonator ($\bar{n} \leqslant 100$). Finally, we get the SNR of the SQUID-embedded resonator with respect to the thermal noise of Josephson parametric amplifier ($150\, mK$) around $0.85/\sqrt{Hz}$. The Tunable SNAIL-embedded resonator can theoretically improve by two orders of magnitude the SNR up to $63.31/\sqrt{Hz}$ even if one uses an HEMT amplifier ($4\, K$).

3 Design and Fabrication

In this section, we will introduce the design of the Tunable SNAIL-embedded CPW resonator and its fabrication process step by step. The designs of the CPW resonator and the SNAIL are shown in Fig.10(a) and Fig.11(b) respectively. This CPW resonator is fabricated by evaporation of a superconducting aluminum layer on a silicon substrate while the SNAIL is fabricated by 2-angle evaporation of aluminum in the middle of the CPW.

3.1 Design of the CPW resonator

The coplanar waveguide is formed by a central conductor with ground planes on both sides and ended by two open circuit terminations. Its designed parameters are chosen to be: f_r =3.75 GHz, $Z_0 = 50\,\Omega$ and $Q \sim 40000$, which fix the dimensions of each component as follows.

3.1.1 Characteristic Impedance

The usual impendance of the coaxial cables is usually chosen to be $50\,\Omega$, which is a good trade-off bewteen the maximum power transfer and minimum losses. We match the characteristic impedance of the CPW to the incoming SMA cable impedance ($Z_0 = 50\,\Omega$) by properly designing the CPW ratio $w/d = 2$ (see in Fig.10(b)) where w is the width of the central conductor and d is the gap between the central conductor and the ground planes:

$$Z_{CPW} = \frac{60\pi}{\sqrt{\varepsilon_{\text{eff}}}\left(\frac{K(k)}{K(k_1)} + \frac{K\left(\sqrt{1-k^2}\right)}{K\left(\sqrt{1-k_1^2}\right)}\right)}$$

And the effective dielectric constant ε_{eff} of the electromagnetic field transferring along the CPW is given by:

$$\varepsilon_{\text{eff}} \approx (1+\varepsilon_r)/2$$

where coefficients $k = w/(w+2d)$, $k_1 = tanh\left(\frac{\pi w}{4h}\right)/tanh\left(\frac{\pi}{4}\frac{w+2d}{h}\right)$ and K is the complete elliptic integral of the first kind[22].

The thickness of our silicon substrate h is 0.3mm ($h \gg w, d$) and its dielectric constant is $\varepsilon_{r,Si} = 11.9$. Therefore, in order to get Z_{CPW} ≈50 Ω, the ratio w/d should be around 2. In our current design, the width of the central conductor is chosen to be $10\,\mu$m and the gap d is $5\,\mu$m(see in Fig.10(c)).

3.1.2 Resonance frequency

The initial resonance frequency of the CPW resonator without SNAIL is aimed to be set at 3.75 GHz which meets operating range of the circuit element (2-4 GHz). As a consequence from last paragraph, the light velocity in the waveguide is $\tilde{c} = c/\sqrt{\varepsilon_{\text{eff}}} \approx 1.17 \times 10^8\, m/s$. We know that the resonator is defined as a $\lambda/2$ segment of a transmission line and the frequency of its first mode is $f_r = \tilde{c}/2L$. Thus, the length of the CPW between the two coupling capacities is given by $L = \tilde{c}/2f_r \approx 15.6\, mm$.

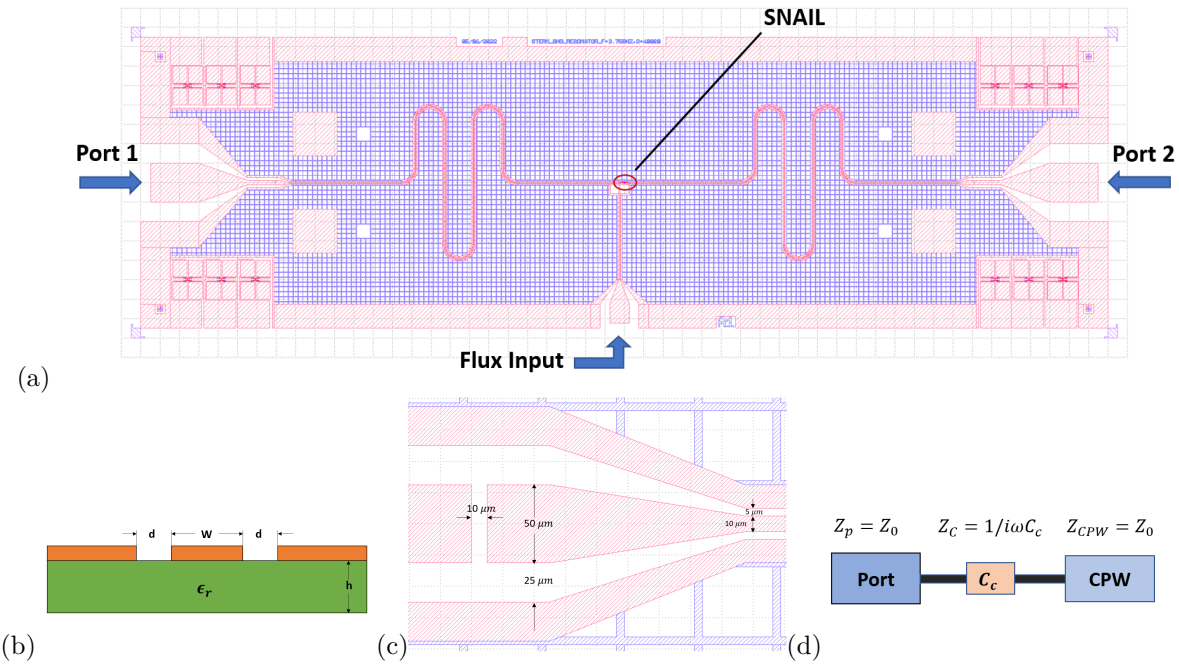

Figure 10: (a) Design of the 3.75 GHz tunable SNAIL Resonator. A flux line allows the local application of a flux in the SQUID loop. (b) Sectional view of a coplanar waveguide with ground planes. The thickness of the substrate h is much larger than the width of the central conductor w and the gap d between the central conductor and the ground. (c) Zoom on the coupling capacitor and on CPW line, the geometry w/d is chosen to be 2. (d) Equivalent circuit used to calculate the quality factor of the resonator.

3.1.3 Quality Factor

The quality factor of the resonator is determined by the transmission coefficient through the open circuit terminations. Consider an incoming wave traveling through this transmission line with a step in impedance from $Z_{left}$to Z_{right}, a portion of the wave will be reflected back with a reflection cofficient R. Due to the continuity of wave transition through termination, the amplitude of transmission wave is therefore given by $1+R$. And the sum of the power in the reflected and transmitted waves should remain unchanged:

$$\frac{1}{Z_{left}} = \frac{R^2}{Z_{left}} + \frac{(1+R)^2}{Z_{right}}$$

The reflection coefficient of the wave is solved by:

$$R = \frac{Z_{right} - Z_{left}}{Z_{right} + Z_{left}} = \frac{Z_0 - \left(Z_0 + \frac{1}{j\omega_r c_c}\right)}{Z_0 + \left(Z_0 + \frac{1}{j\omega_r c_c}\right)} = \frac{1}{2jC_c\omega_r Z_0 + 1}$$

Since our resonator has a high quality factor, the transmission coefficient $T = 1 - |R|^2 \ll 1$ is:

$$T = 1 - \frac{1}{1 + 4C_c^2\omega^2 Z_0^2} \approx 4C_c^2\omega_r^2 Z_0^2$$

The quality factor due to the capacitor on both sides are given by $Q_{l/r} = \frac{2\pi}{T_{l/r}}$,and the total quality

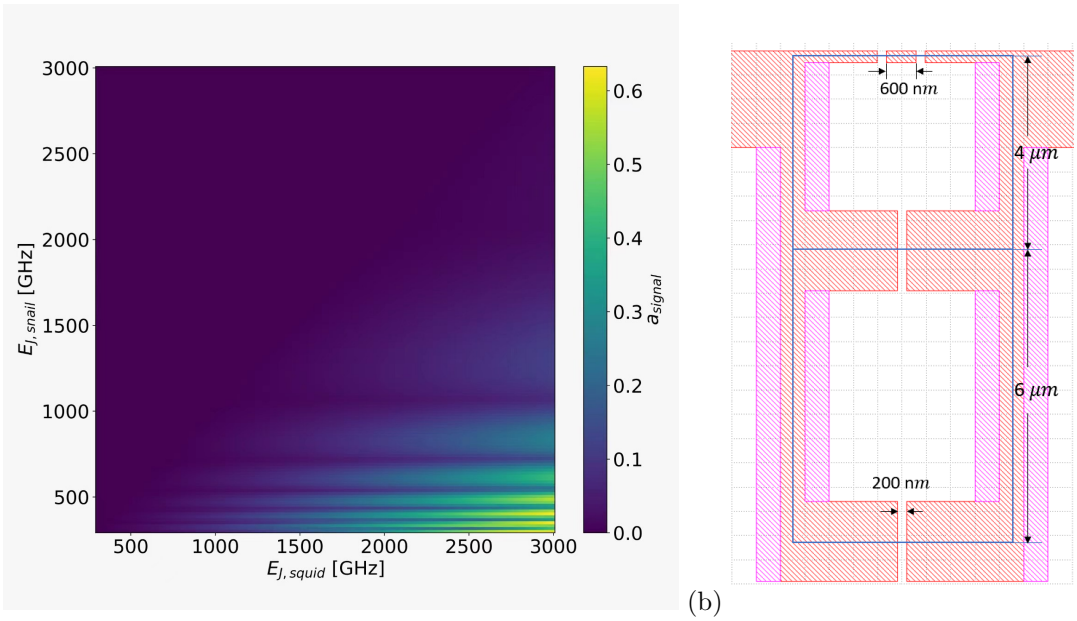

(a) (b)

Figure 11: (a) The amplitude of simulated signal a_{signal} versus the Josephson energy of the unitary junctions $E_{J,snail}$ and of the SQUID's junctions $E_{J,squid}$. (b) Ebeam lithography design of the SNAIL with $E_{J,snail} = 2000\,GHz$ and $E_{J,squid} = 300\,GHz$. The pink shaded area is proposed to be exposed with less time which creates the undercut below the ebeam mask.

factor of the system is given by:

$$\frac{1}{Q} = \frac{1}{Q_l} + \frac{1}{Q_r} = \frac{4C_c^2\omega_r^2 Z_0^2}{\pi}$$

while $C_{c,l} = C_{c,r}$ .The quality factor of the resonator is designed to be $Q = 40000$, therefore we obtain a coupling capacitor C_c

$$C_c = \sqrt{\frac{\pi}{4Q}}\frac{1}{\omega_r Z_0} \approx 3.8\ \text{fF}$$

The dimensions of the coupling capacitor have been calculated with by Sonnet (an electromagnetic simulating software). According to Sonnet, two pads of 50 μmwidth separated by a 10 μmgap (see in Fig.10(c)) give rise to a coupling capacitor $C_c \approx 3.8$ fF.

3.2 Design of the Tunable SNAIL

According to the simulation results shown in Fig.11(a), a good choice for the Josephson energies of the SNAIL unitary junctions $E_{J,snail}$ is $300\,GHz$ (corresponding to a critical current of $\sim 600\,nA$) and for the symmetric SQUID's junctions $E_{J,squid}$ is $2000\,GHz$ (corresponding to a critical current of $\sim 4\,uA$). Their resistance can be extracted by using Ambegaokar-Baratoff formula[23]:

$$I_c = \frac{\pi\Delta}{2eR}$$

where $\Delta \approx 210\,\mu eV$ is the superconducting gap of a thin layer of aluminum with thickness 30nm at 4K [24].

The product of the resistance and the areas of the aluminum junction fabricated on the silicon is typically given by $R * S_{jun} = 25\Omega * \mu m^2$. Thus, the area of the two kinds of junctions is extracted by 0.0495 μm^2 and 0.3301 μm^2. These junctions will be fabricated by 2 angle evaporation and the displacement is chosen to be 400 nm and results in a 200 nm width overlap, thus their length are given by 0.248 μm and 1.65 μm respectively.

3.3 Fabrication of the tunable SNAIL-embedded Resonator

In the following tables, we will present the different steps of the fabrication process of the tunable SNAIL-embedded resonator.

3.3.1 Dicing - cut the wafer to square

For convenience, we first dice the 2 inch silicon wafer into coupons before further process. The coupon's size is chosen to be 1 inch square and each one will contain 14 samples with dimensions $10mm \times 3mm$.

Step #	Process Name	Process Content
1	Spin Coating	Photo-resist AZ1512 500rpm 5s, 5000rpm 60s, 6000rpm 2s
		Hot plate, 100°C 1min
		Re-coat as before and bake at 100°C 5mins
2	Dicing	Front dicing in three steps, every step remove 140μm
3	Cleaning	Piranha acid 10mins, water, IPA, N_2 Blow-dry

3.3.2 Alignment marks

The SNAIL is aimed to be inserted in the middle of the CPW, thus alignment marks are needed to help align the SNAIL with the resonator. We choose Niobium marks due to their good visibility under electron beam and their resistance to the Piranha acid cleaning.

Step #	Process Name	Process Content
1	Evaporation	130nm Nb layer evaporated on silicon substrate.
2	Prebake	Hot plate, 180°C 2mins
3	Spinning Resist	Photo-resist AZ1512 500 rpm 5s, 5000 rpm 60s, 6000 rpm 2s
4	Soft Bake	Hot plate, 100°C 1min
5	UV Lithography	Dose 25, Defoc 0, CD -200 -200
6	Development	AZ726 90s, water 30s+
7	Microscope	See whether MLA is good, if not repeat
8	Hard bake	Hot plate, 120°C 5mins
9	Reactive Ion Etch	Stick the sample in the middle of the wafer
		Focus the laser on the Nb
		Al BCl_Cl etch, stop before all the Nb be eaten
10	HF Etch	HF acid 30mins, water, IPA, N_2 Blow-dry
11	Cleaning	Piranha acid 10mins, water, IPA, N_2 Blow-dry

3.3.3 UV Lithography

After fabricating the aliment marks, we begin to fabricate the CPW resonator by UV lithography. The fabrication of the resonator is done by using Al-etchant to remove an evaporated 150 nm layer of aluminum according to a photoresist mask.

Step #	Process Name	About the process
1	Evaporation	150nm Aluminum layer evaporation
2	Heating	Hot plate, 180°C 2mins
3	Spinning resist	Photo-resist $AZ1505$, 500rpm 2s, 5000rpm 60s, 6000rpm 2s
4	Soft bake	Hot plate, 80°C 5mins
5	UV lithography	MLA150, Dose=22 [mJ/cm^2], inversion on, CD -600, Defocus -2
6	Development	AZ726 45s, Water 45s, N_2 Blow Dry 45s
7	Microscope	See whether MLA is good, if not, repeat
8	Hard bake	Hot plate, 120°C 5mins
9	Etching	Wait Al etching until see homogeneous by eyes, 1min more
		Water 90s, AZ726 1min, Water 90s, N_2 Blow Dry 90s
10	Cleaning	NMP, 85°C over night, Water, IPA, N_2 Blow Dry
11	Microscope	Check the sample for unwanted shorts or resist particles remained

3.3.4 Tri-layer protocol

The fabrication of the SNAIL is made by a so-called Tri-layer protocol[25]. A germanium mask is created by Ebeam lithography and subsequent SF6 etching. The advantage of this technique is that the mask is rigid, evacuates efficiently the charges and is robust to cleaning by oxygen ashing.

Step #	Process Name	About the process
1	Heating	Hot plate, 180°C, 5 $\sim$ 10mins
2	Spin Coating	MAA 8.5 EL7, use syringe filters, 500rpm 2s, 2000rpm 60s
		Hot plate, 180°C 1 min
		Re-coat as before and bake at 180°Cfor 15mins
3	Evaporation	60nm Ge layer
4	Spinning resist	CSAR resist, use syringe filters, 500rpm 2s, 4500rpm 60s
5	Post bake	Hot plate, 100°C 5mins
6	Ebeam lithography	Dose=666[uC/cm^2], 30pA for real design, 250pA for big pads
7	Development	*IPA:MIBK* 4mins, *IPA* 1min
8	RIE	SF6 slow recipe, use a second sample for calibration
		Record the time of Etch
		Wait more 80% of the time (up to 200%)
9	Development	*IPA:MIBK* 90s, *IPA* 90s, N_2 Blow Dry
10	Plasma Etching	$O_2 + N_2$ ashing 50% 3mins
11	AFM	Measure the step height H (Ge+MAA), usually $660 \pm 20nm$

3.3.5 Cold Evaporation

Before the evaporation, we first need to calculate the evaporation angle $\pm\theta$ relative to the sample axis. As mentioned earlier, the displacement between 2 evaporation layers is chosen to be 400nm, the evaporation angle is therefore given by $\theta = arctan(200nm/H)$. The Ion milling step removes the oxide layer from the central conductor of the resonator in order to establish a good galvanic contact between the SNAIL and the central conductor of the resonator.

Step #	Process Name	About the process
1	Ion milling	25° 5s, −25° 5s
2	Cool down	Liquid N_2, −50°C
3	1st Evaporation	20nm layer, −44°C, $-\theta$
4	Dynamic oxidation	$-10°C \sim 4°C$, pressure around 0.02mbar
5	2nd Evaporation	20nm layer, $4° \sim 10°C$, θ
6	Static oxidation	10mins, above$10°C$
7	Cleaning	NMP, $85°C$ over night, Water, IPA, $N2$ Blow Dry

3.4 Room temperature characterization

At the end of the fabrication process, we observe the quality of our sample by using an Atomic Force Microscope (AFM). The AFM scan has an ultra-high resolution and allows us to extract critical information on the sample such as the shape of the SNAIL, the dimensions of the junctions, the presence of remaining particles of resist on the surface of the sample... . Fig.12(a) presents an AFM micrograph of one of the measured sample, the dimensions of each unitary junction are reproducible and the asymmetry of the SQUID is close to 0.

The I-V characteristic of test junctions at room temperature should be performed before measuring the resonator at low temperature inside the dilution refrigerator. The test junctions are fabricated simultaneously with the tunable SNAIL and we assume that the resistance of these test junctions is similar to the ones of the true device. The resistance measurement are performed by using a probe station based on four-terminal sensing (see in Fig.12(b)).

In Fig.12(c), we present 2 histograms showing the resistance distribution of the test junctions. The bin in these 2 different histograms represent 5 Ω and 20 Ω width respectively, and its height represents the number of junctions tested inside this range. The statistics of the test junctions presented here were taken from 100 test junctions where half of them are SQUID large junctions (blue) and the rest are unitary SNAIL junctions (red).

The average resistance of the SQUID junctions and SNAIL junctions are 109.53 Ω and 564.03 Ω, respectively with standard deviations 6.68% and 5.72%, which more or less meets our requirements. Using Ambegaokar relation, we can extract the critical current of the junctions : $I_{c,unitary} = 2.80 \pm 0.19\ \mu A$ and $I_{c,squid} = 0.54 \pm 0.03\ \mu A$.

After these measurements, we dice our coupon into 14 samples ($10mm \times 3mm$) and select the best one for low temperature measurement. In order to protect the samples during dicing, we spin the front side of the coupon with three layers of PMMA, that is removed in NMP after dicing. Then the sample is glued and bonded to a PCB holder, which is embedded in an OHFC copper box.

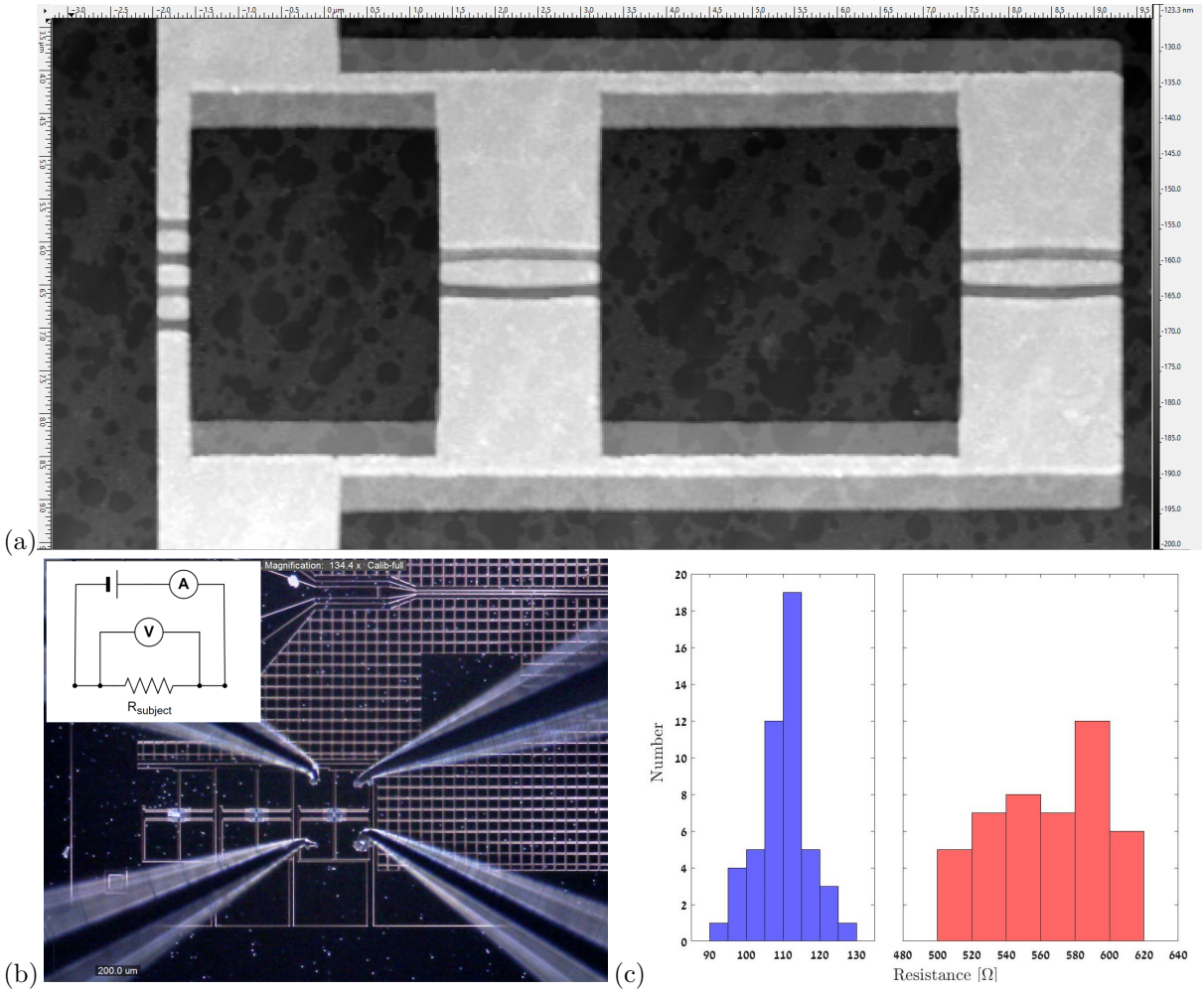

Figure 12: (a) An AFM micrograph of a tunable SNAIL. (b) Microscope picture of the probe station measuring the resistance with the equivalent electrical scheme showing on the top left. (c) Test junction resistance histograms representing the resistance distribution of 50 test SQUID large junctions (blue) and 45 unitary SNAIL junctions (red).

4 Experimental Setup

The measurements described herein below (see in Fig.13) have been performed in the lab of S. Rosenblum at Weizmann Institute due to a major breakdown of our dilution fridge. This breakdown required sending the fridge back to the supplier for repair.

As mentioned in last section, our sample is embedded in an OHFC copper box and now is placed inside a superconducting coil, which is used to produce a homogeneous magnetic field, in the 20 mK stage of the dilution refrigerator. In order to protect the SNAIL from environmental magnetic field fluctuations, the superconducting coil is placed inside two layers of protecting shields: the first layer is made out of Titanium and acts as a superconducting shield while the second layer is made out of Cryoperm, which is a mu-metal working at low temperatures . Outside the fridge, the coil is connected to a BILT voltage DC source that is connected in series with a 5kΩ resistor in order to provide a well controlled DC current.

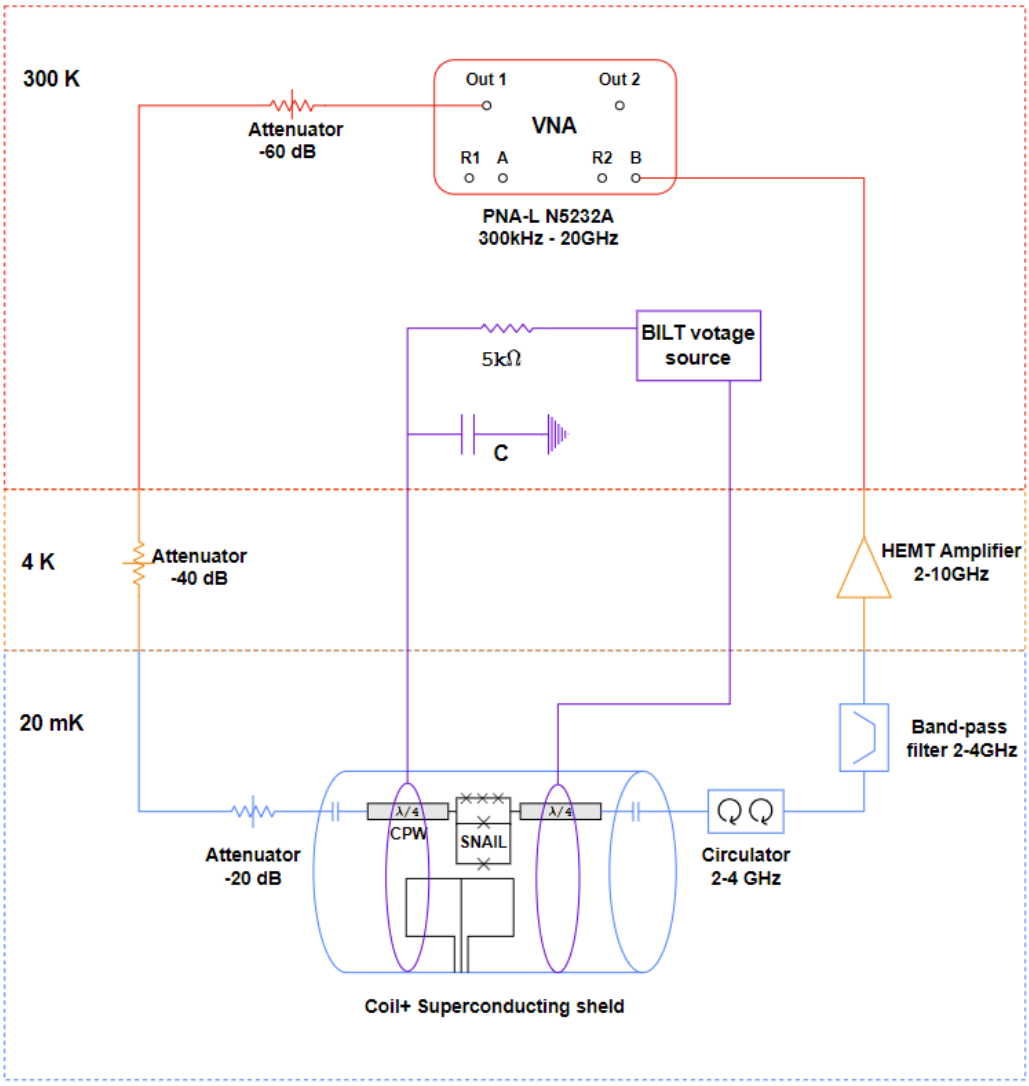

(a)

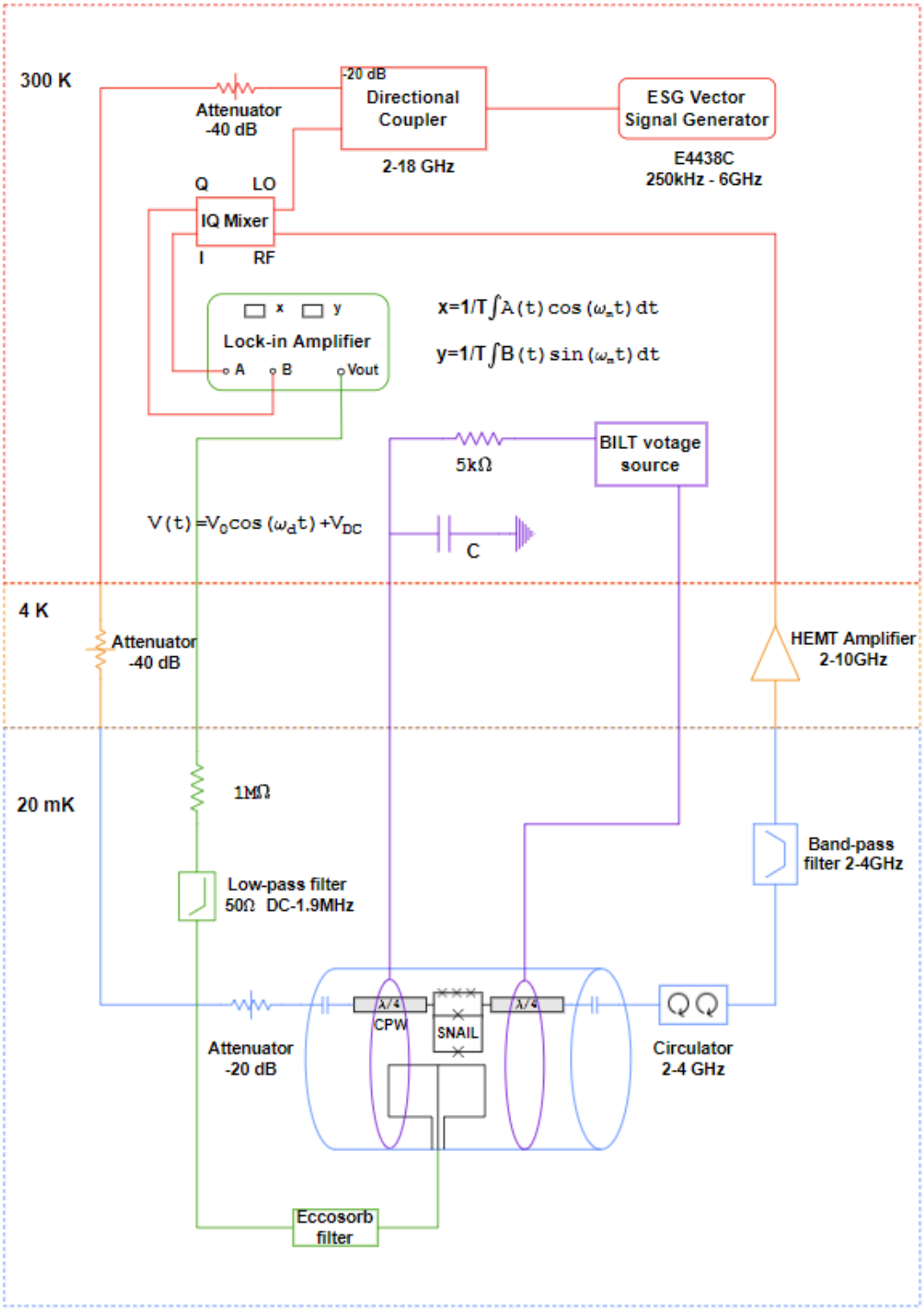

(b)

Figure 13: A scheme of the experimental setup. (a) Sub-scheme of the VNA measurement. (b) Sub-scheme of the Lock-in measurement.

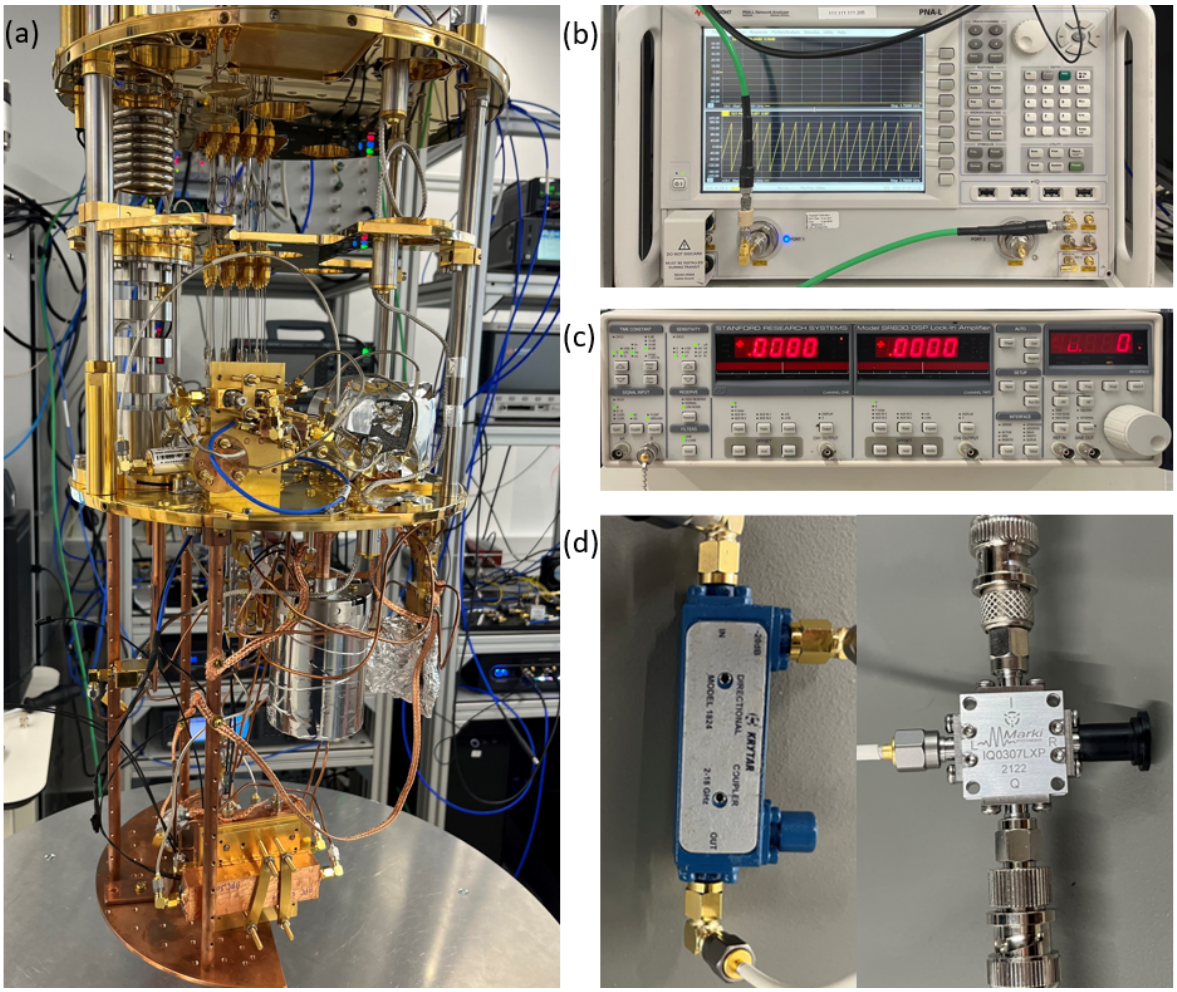

Figure 14: Pictures of the measuring system. (a) Picture of a ^3He dilution refrigerator. (b) Picture of a Keysight PNL Vector Network Analyzer (VNA). (c) Picture of a Lock-in amplifier. (d) Picture of a directional coupler and a IQ mixer.

In a first experiment, the input microwave signal is generated from a Keysight PNL Vector Network Analyzer (VNA) and attenuated by $-60\,dB$ at room temperature and $-40\,dB$ at various stages up to $20\,mK$. In order to get rid of the influence of remaining thermal incoming noise , a low temperature attenuator of $-20\,dB$ is added and located at the $20\,mK$ stage. At the output port of the resonator, we use a circulator that passes the signal from the resonator but blocks by $\sim 50\,dB$ incoming thermal noise from the amplifier. The transmission signal is then amplified by a HEMT amplifier and finally detected by the second port of the VNA.

In the second experiment, the microwave signal is generated by an ESG Vector Signal Generator and split by a directional coupler where 1% of the signal is transmitted to the input port of the resonator and the rest is used as a LO reference port of an IQ mixer. An AC magnetic field is generated in the SQUID loop by pushing an A.C current a flux line situated in the vicinity of the SQUID. This AC current is generated by the AC internal voltage source of the Lock-in SRS830 amplifier at a frequency of $1019\,Hz$. The signal passing through the sample is first demodulated by the IQ mixer. Then the I/Q signal is inserted in the Lock-in amplifier and demodulated at the reference frequency of the lock-in.

5 Preliminary Results

5.1 Transmission of the resonator

A first measurement of the resonator transmission is operated by a VNA when the DC current flowing in the coil is zero. In Fig 15(b), we present the frequency scan (blue) and its fit (red) depending on a transmission equation:

$$|S_{21}|^2 = \left(\frac{Q_t}{Q_c}\right)^2 \frac{1}{1 + 4Q_t^2\left(\frac{f-f_r}{f_r}\right)}$$

The obtained parameters $f_r = 3.7345\,GHz$, $Q_t = 33570$ in agreement with our fabrication design.

Then, we sweep the DC current flowing in the coil is comprised between $-2.4 \sim 2.4\,mA$. When the magnetic flux generated by the coil is at the vicinity of the optimal point of the SNAIL ($\Phi_{ext,snail} = k\Phi_0/3$, got from the simulation shown in Appendix), the resonance frequency of the resonator ω_r will shift downwards. As shown in Fig.15(a), the neighborhood of each dip is unclear due to the quality factor decrease. We make a close-up scan of each dip with improved bandwidth ($5\,Hz$) and resolution ($0.01\,MHz$), which allows a better detection of the depth of the dips.

Fig.15(e) represents the transmission in response to the effect of power when the DC magnetic flux is set close to the dip. The resonance frequency's shifts to lower frequency when the driving power is increased as one can expect from Kerr nonlinearity. A bifurcation point is occurred at $P_{in} = -121.2dBm$, where the photons stored inside the resonator is therefore given by $\bar{n} \sim 1000$.

5.2 Lock-in measurement

Once we finished the DC scan of the magentic flux and accumulated the information of optimal point, we begin to use Lock-in amplifier and generate a tiny AC magnetic flux in the SQUID. Such AC magnetic flux will modulate the resonator's resonance frequency and will be manifested by a small shift of the output signal.

Here, we use an ESG Vector Signal Generator generate the microwave source and sweep frequencies between 3.25 and $3.75\,GHz$ (501 points). The amplitude of the Lock-in amplifier's AC voltage is chosen between $4\,mV$ and $100\,mV$ (where we could see heating effects on the fridge) and its frequency is chosen to be $1019\,Hz$. As shown in Fig.13(b), the signal passing through the sample is first demodulated by the IQ mixer, where the LO reference is locked in input microwave source. Then the I/Q signal is inserted in the Lock-in amplifier, synchronized to a modulation at same frequency. When the frequency sweeps approach the resonance frequency of the resonator, we will observe the peak of R.

Unfortunately, a ground loop in the fridge at Weizmann was discovered during our measuring session. This technical problem can be solved easily in the future. We are currently waiting for the opening of the refrigerator and will then try to fix this problem and remeasure our sample in a few weeks.

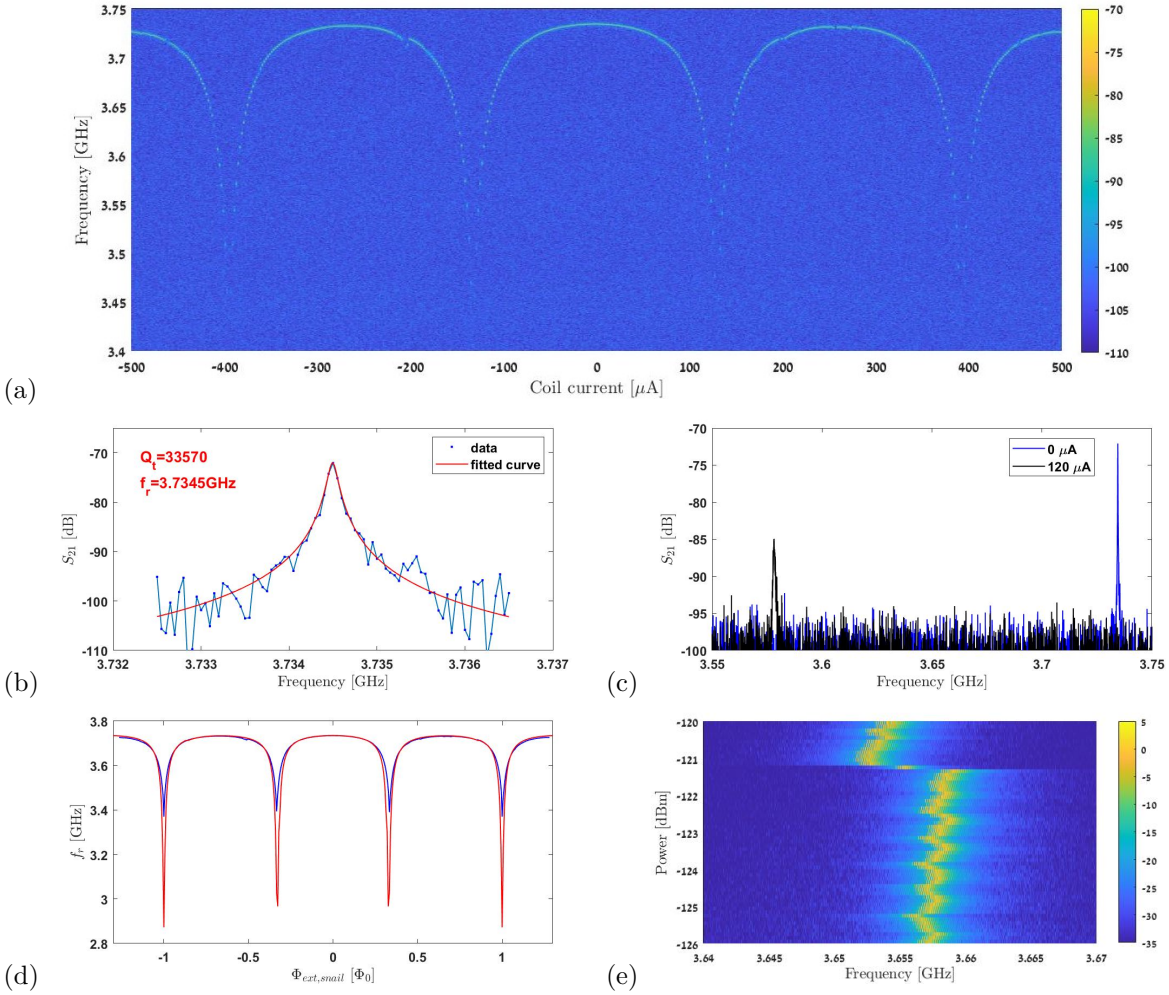

Figure 15: (a) A 2D color plot of S_{21} as a function of coil current and scanning frequency. (b) S_{21} versus scanning frequency (blue) and fitted function (red) with $\Phi_{ext} = 0$ and input power $P_{in} = -125\,dBm$. (c) Extracted resonance frequency of the resonator versus coil current. (d) Resonance frequency f_r versus magentic flux threading inside SNAIL $\Phi_{ext,snail}$ (blue) and the theoretical simulation curve (red) with asymmetry is set to d=0.01 (other parameters are set as same as expermental results). (e) 2D plot of S_{21} versus scanning frequency and driving power. The resonance frequency shifts upwards slowly in response to the grow of driving power till bifurcation point, then the resonance frequency will jump immediately.

6 Discussion and Conclusion

The DC SQUID is one of the most popular and established technique used for detection and characterization of tiny weak magnetic fields. Yet, the resolution and bandwidth of this device is intrinsically limited by the dissipation in the shunt resistor at subkelvin temperatures.

Siddiqi et al. have recently developed a dispersive nanoSQUID magnetometer by using a SQUID embedded in the middle of the CPW resonator[13]. At low power, the system forms essentially a harmonic oscillator with a flux dependent resonance frequency, which can be used to detect the low frequency AC flux threaded inside the SQUID loop. The major problem of this technique is that if one pump too strongly the resonator in order to improve he signal to noise ratio, the effect of Kerr non-linearity (φ^4) and sensitivity loss can't be neglected.

In this research, we replaced the SQUID by a tunable SNAIL, which can be considered as a pure φ^3 nonlinear element and thus prevent nonlinear effect up to sixth order. We design, fabricate, and measure a new kind of SNAIL whose α junction is substituted by a symmetric SQUID. We believe that this new technique based on tunable SNAIL will show a great advantage of SNR when compared with SQUID and have shown interesting preliminary results towards this goal. More measurements are required in order to conclude this research.

Due to problems with the dilution refrigerator, we failed in measuring the signal by Lock-in amplifier until now.

References

[1] JE Zimmerman and AH Silver. Macroscopic quantum interference effects through superconducting point contacts. *Physical Review*, 141(1):367, 1966.

[2] John Clarke and Alex I Braginski. *The SQUID handbook*, volume 1. Wiley Online Library, 2004.

[3] Michael Tinkham. *Introduction to Superconductivity*. Dover Publications, 2 edition, June 2004.

[4] Frederick C Wellstood, Cristian Urbina, and John Clarke. Low-frequency noise in dc superconducting quantum interference devices below 1 k. *Applied Physics Letters*, 50(12):772–774, 1987.

[5] Jochen Braumüller, Leon Ding, Antti P Vepsäläinen, Youngkyu Sung, Morten Kjaergaard, Tim Menke, Roni Winik, David Kim, Bethany M Niedzielski, Alexander Melville, et al. Characterizing and optimizing qubit coherence based on squid geometry. *Physical Review Applied*, 13(5):054079, 2020.

[6] E Paladino, L Faoro, G Falci, and Rosario Fazio. Decoherence and 1/f noise in josephson qubits. *Physical review letters*, 88(22):228304, 2002.

[7] Yu M Galperin, BL Altshuler, and DV Shantsev. Low-frequency noise as a source of dephasing of a qubit. In *Fundamental Problems of Mesoscopic Physics*, pages 141–165. Springer, 2004.

[8] F Yoshihara, K Harrabi, AO Niskanen, Y Nakamura, and Jaw Shen Tsai. Decoherence of flux qubits due to 1/f flux noise. *Physical review letters*, 97(16):167001, 2006.

[9] Jonas Bylander, Simon Gustavsson, Fei Yan, Fumiki Yoshihara, Khalil Harrabi, George Fitch, David G Cory, Yasunobu Nakamura, Jaw-Shen Tsai, and William D Oliver. Noise spectroscopy through dynamical decoupling with a superconducting flux qubit. *Nature Physics*, 7(7):565–570, 2011.

[10] Michael Stern, Gianluigi Catelani, Yuimaru Kubo, Cecile Grezes, Audrey Bienfait, Denis Vion, Daniel Esteve, and Patrice Bertet. Flux qubits with long coherence times for hybrid quantum circuits. *Physical review letters*, 113(12):123601, 2014.

[11] M Hatridge, R Vijay, DH Slichter, John Clarke, and I Siddiqi. Dispersive magnetometry with a quantum limited squid parametric amplifier. *Physical Review B*, 83(13):134501, 2011.

[12] EM Levenson-Falk, R Vijay, N Antler, and I Siddiqi. A dispersive nanosquid magnetometer for ultra-low noise, high bandwidth flux detection. *Superconductor Science and Technology*, 26(5):055015, 2013.

[13] EM Levenson-Falk, N Antler, and I Siddiqi. Dispersive nanosquid magnetometry. *Superconductor Science and Technology*, 29(11):113003, 2016.

[14] Crispin W Gardiner and Matthew J Collett. Input and output in damped quantum systems: Quantum stochastic differential equations and the master equation. *Physical Review A*, 31(6):3761, 1985.

[15] Aashish A Clerk, Michel H Devoret, Steven M Girvin, Florian Marquardt, and Robert J Schoelkopf. Introduction to quantum noise, measurement, and amplification. *Reviews of Modern Physics*, 82(2):1155, 2010.

[16] R Vijay, MH Devoret, and I Siddiqi. Invited review article: The josephson bifurcation amplifier. *Review of Scientific Instruments*, 80(11):111101, 2009.

[17] NE Frattini, U Vool, S Shankar, A Narla, KM Sliwa, and MH Devoret. 3-wave mixing josephson dipole element. *Applied Physics Letters*, 110(22):222603, 2017.

[18] NE Frattini, VV Sivak, A Lingenfelter, S Shankar, and MH Devoret. Optimizing the nonlinearity and dissipation of a snail parametric amplifier for dynamic range. *Physical Review Applied*, 10(5):054020, 2018.

[19] TP Orlando, JE Mooij, Lin Tian, Caspar H Van Der Wal, LS Levitov, Seth Lloyd, and JJ Mazo. Superconducting persistent-current qubit. *Physical Review B*, 60(22):15398, 1999.

[20] I Chiorescu, Y Nakamura, CJP Ma Harmans, and JE Mooij. Coherent quantum dynamics of a superconducting flux qubit. *Science*, 299(5614):1869–1871, 2003.

[21] J Bourassa, F Beaudoin, Jay M Gambetta, and A Blais. Josephson-junction-embedded transmission-line resonators: From kerr medium to in-line transmon. *Physical Review A*, 86(1):013814, 2012.

[22] Brian C Wadell. *Transmission line design handbook*. Artech House Microwave Library, 1991.

[23] Vinay Ambegaokar and Alexis Baratoff. Tunneling between superconductors. *Physical Review Letters*, 10(11):486, 1963.

[24] AJ Ferguson, RG Clark, et al. Energy gap measurement of nanostructured aluminium thin films for single cooper-pair devices. *Superconductor Science and Technology*, 21(1):015013, 2007.

[25] T Chang, T Cohen, I Holzman, G Catelani, and M Stern. Tunable superconducting flux qubits with long coherence times. *arXiv preprint arXiv:2207.01460*, 2022.

[26] John Clarke and Roger H Koch. The impact of high-temperature superconductivity on squid magnetometers. *Science*, 242(4876):217–223, 1988.

[27] Grégoire Ithier. *Manipulation, readout and analysis of the decoherence of a superconducting quantum bit*. PhD thesis, Université Pierre et Marie Curie-Paris VI, 2005.

[28] K Segall, C Wilson, L Li, L Frunzio, S Friedrich, MC Gaidis, and DE Prober. Dynamics and energy distribution of nonequilibrium quasiparticles in superconducting tunnel junctions. *Physical Review B*, 70(21):214520, 2004.

[29] Amit Finkler, Yehonathan Segev, Yuri Myasoedov, Michael L Rappaport, Lior Neeman, Denis Vasyukov, Eli Zeldov, Martin E Huber, Jens Martin, and Amir Yacoby. Self-aligned nanoscale squid on a tip. *Nano letters*, 10(3):1046–1049, 2010.

[30] Denis Vasyukov, Yonathan Anahory, Lior Embon, Dorri Halbertal, Jo Cuppens, Lior Neeman, Amit Finkler, Yehonathan Segev, Yuri Myasoedov, Michael L Rappaport, et al. A scanning superconducting quantum interference device with single electron spin sensitivity. *Nature nanotechnology*, 8(9):639–644, 2013.